Recently Amplified Interannual Variability of the Great Lakes Ice Cover in Response to Changing Teleconnections

YU-CHUN LIN,[a] AYUMI FUJISAKI-MANOME,[b,c] AND JIA WANG[d]

[a] *Center of Excellence for Ocean Engineering, National Taiwan Ocean University, Keelung City, Taiwan*
[b] *Cooperative Institute for Great Lakes Research, University of Michigan, Ann Arbor, Michigan*
[c] *Climate and Space Sciences and Engineering, University of Michigan, Ann Arbor, Michigan*
[d] *Great Lakes Environmental Research Laboratory, NOAA, Ann Arbor, Michigan*

(Manuscript received 10 June 2021, in final form 7 June 2022)

ABSTRACT: The interannual variability of the annual maximum ice cover (AMIC) of the Great Lakes is strongly influenced by large-scale atmospheric circulations that drive regional weather patterns. Based on statistical analyses from 1980 to 2020, we identify a reduced number of accumulated freezing degree days across the winter months in recent decades, a step-change decrease of AMIC after the winter of 1997/98, and an increased interannual variability of AMIC since 1993. Our analysis shows that AMIC is significantly correlated with El Niño–Southern Oscillation (ENSO), the North Atlantic Oscillation (NAO), and the Pacific–North American pattern (PNA) before the winter of 1997/98. After that, the AMIC is significantly correlated with the tropical–Northern Hemisphere pattern (TNH) and eastern Pacific oscillation (EPO). Singular value decomposition of the 500-hPa geopotential height and surface air temperature shows a dipole pattern over the northeast Pacific and North America, demonstrating the ridge–trough system. This dipole pattern shifts northward to the northern Rocky Mountains, placing the Great Lakes region in the trough after 1997/98. This shift coincides with the increased interannual variability of the EPO index, as well as the change in the sea surface temperature (SST) over the northeast Pacific, where the second mode of the empirical orthogonal function (EOF) on SST shows a warm blob-like feature manifested over the Gulf of Alaska. The regression of wave activity flux onto the SST EOF shows that the source of upward and eastward propagation of a stationary Rossby wave shifts to the west coast of North America, likely moving the ridge–trough system eastward after the winter of 1997/98.

SIGNIFICANCE STATEMENT: We found that the Great Lakes annual maximum ice cover decreased after one of the strongest El Niño–Southern Oscillation events in 1997/98 and that its year-to-year fluctuations increased in the recent 20 years. After the winter of 1997/98, the Great Lakes annual maximum ice cover started to correlate with the warm sea surface temperature anomaly in the northeast Pacific, which appears to disrupt the polar vortex far up in the stratosphere, and the polar vortex ultimately shifts eastward the ridge–trough system over North America. When the shifted system develops enough, it can encase the Great Lakes region in the Arctic air and thereby cause larger year-to-year fluctuations. This connection was found to be characteristic in the recent few decades, after the winter of 1997/98.

KEYWORDS: North America; Atmospheric circulation; ENSO; Indices; Pacific-North American pattern/oscillation; Teleconnections

1. Introduction

The North American Great Lakes (hereafter simply the Great Lakes) account for ~20% of the world's freshwater. The Great Lakes are partially frozen each year with large year-to-year fluctuations. Annual maximum ice cover (AMIC) is defined as the measured maximum daily ice cover of the Great Lakes in an ice season (winter). Extremely cold winters with high AMIC have substantial impacts on the surrounding population (Assel et al. 1996, 2000), the economy (Niimi 1982), under-ice ecosystems (Vanderploeg et al. 1992; Magnuson et al. 1995), and winter limnology in general (Ozersky et al. 2021). Studies have shown that the ice cover of all five lakes has decreased in recent decades in response to global warming (Magnuson 2000; Wang et al. 2012; Titze and Austin 2014).

Recent studies have shown evidence of Arctic–midlatitude interactions that influence winter weather conditions over Eurasia and North America (Honda et al. 2009; Liu et al. 2012; Cohen et al. 2014; Ogi et al. 2015; Francis et al. 2009; Wang et al. 2018). Arctic surface air temperature in winter rose significantly after 1998, where the trends have been stronger over the Barents–Kara Seas and East Siberian–Chukchi Seas, and the warm Arctic surface air temperature has often been observed to follow a reduction of autumn sea ice (Kug et al. 2015). Honda et al. (2009) proposed that such a connection was caused by the stationary Rossby waves, providing a "warm Arctic–cold continent" pattern (Overland et al. 2011). Recent studies have shown that such a warm Arctic–cold continent pattern over North America was partly (~50%) driven by the sea surface temperature (SST) pattern in the North Pacific (Guan et al. 2021). Moreover, the combination of sea ice loss in the Bering Sea and the SST over the western

Denotes content that is immediately available upon publication as open access.

Corresponding author: Yu-Chun Lin, yuchlin@mail.ntou.edu.tw

DOI: 10.1175/JCLI-D-21-0448.1

tropical Pacific strongly affected the winter of 2013/14 (Lee et al. 2015), which coincided with one of the largest AMICs in recent years, also suggesting the important roles of Pacific SST on the variation of Great Lakes ice cover. On the other hand, the direct connections between Arctic amplification and the midlatitude extreme weather were found to be insignificant (Barnes 2013; Barnes and Polvani 2015). Furthermore, the contributions from Arctic sea ice loss, especially over the Bering and Chukchi Seas, to the midlatitudes through blocking planetary waves, jet stream waviness, and weakening the polar vortex were reported to be minor or insignificant (Cohen et al. 2014; Blackport and Screen 2020).

The variations of the AMIC have been mostly in response to the combinations of regional and Northern Hemisphere climate patterns. In the past decades, studies were conducted to investigate the relationships between Great Lakes AMIC and teleconnections, including El Niño–Southern Oscillation (ENSO), the Pacific–North American teleconnection pattern (PNA), the Pacific decadal oscillation (PDO), the tropical–Northern Hemisphere pattern (TNH), the North Atlantic Oscillation (NAO), and the Arctic Oscillation (AO), through their influences on the weather conditions over North America (Smith 1991; Hanson et al. 1992; Assel and Robertson 1995; Assel 1998; Rodionov and Assel 2000, 2001; Assel et al. 2003; Wang et al. 2010, 2012, 2018; Budikova et al. 2021). Almost half of the low AMIC events were associated with strong positive ENSO events (Assel 1998; Assel and Rodionov 1998) and had high positive correlations with the PNA and TNH (Assel 1992; Assel and Rodionov 1998). Budikova et al. (2021) found similar effects of the PNA and the TNH on the winter in North America by conducting analyses on a half-century-long winter severity index, which was calculated from daily records of snowfall, snow depth, and air temperature difference. The NAO/AO was found to partially contribute to ice cover in some areas of the Great Lakes (Assel et al. 1985, 2000; Rodionov and Assel 2001). Recent studies have also shown that the variability of AMIC is correlated linearly to the NAO and nonlinearly to ENSO at the same time (Bai et al. 2012), which complicates the diagnosis of the weather circulations related to Great Lakes ice cover. At longer time scales, studies have shown that the AMIC is weakly and positively related to the PDO (Wang et al. 2018). These works suggest the complexity between the teleconnection patterns related to climate indices and the winter surface air temperature as well as the subsequent AMIC of the Great Lakes.

AMIC has experienced extremely high and low conditions in recent years (Fig. 1a), especially after the late 1990s (Van Cleave et al. 2014). The extreme cold winter in 2013/14, one of the most notable events, was characterized by numerous cold air outbreaks (Huntingford et al. 2015) and was impacted by the SST anomaly over the central tropical and North Pacific (Hartmann 2015; Lee et al. 2015; Wang et al. 2015; Guan et al. 2021). Such extreme winter conditions over the Great Lakes in recent years, particularly in terms of how they relate to the larger atmospheric circulations, have not yet been discussed and are not fully understood. In this study, we examine the time series of AMIC over the past few decades, how it correlates with select climate indices and larger-scale atmospheric circulations, and the mechanisms that could impact the winter surface air temperature and the accumulated freezing degree days (AFDDs) over the Great Lakes region.

2. Data and methods

AMIC is defined as the maximum daily ice cover (percentage of lake surface area) in the Great Lakes each winter. We obtained the AMIC data from 1980 to 2020 from the National Oceanic and Atmospheric Administration/Great Lakes Environmental Research Laboratory (NOAA/GLERL) Ice Atlas database (Wang et al. 2017; Yang et al. 2020). We obtained the monthly gridded Arctic sea ice concentration from the HadISST1.1 (Met Office Hadley Center), which showed a spatial resolution of 1° × 1° (Rayner et al. 2003). We obtained monthly atmospheric data from 1979 to 2020, including geopotential height at 500 hPa (Φ500) and surface air temperature at 2-m height (T_{2m}), from the National Centers for Environmental Prediction–Department of Energy Atmospheric Model Intercomparison Project II (NCEP Reanalysis II; Kanamitsu et al. 2002), which has a spatial resolution of 2.5° × 2.5°. AFDDs, which are defined as the summation of averaged daily temperature below freezing degrees (0°C) for a specified period, around the Great Lakes region were chosen to represent the winter severity from November to February (Assel et al. 2004; Wang et al. 2020). The AFDDs around the Great Lakes are linked with AMIC (Rogers 1976; Wang et al. 2020) and can improve 30-day forecast of the Great Lakes ice cover (Assel et al. 2004).

We selected the monthly climate indices of ENSO (Barnston et al. 1997), PDO (Mantua et al. 1997), NAO (Hurrell 1995), AO (Thompson and Wallace 1998), PNA (Barnston and Livezey 1987), and TNH (Mo and Livezey 1986) to examine the connections with AMIC as they were found to influence the weather in the Northern Hemisphere. The eastern Pacific oscillation (EPO; Barnston and Livezey 1987) was also included in this study. The EPO index is defined based on the difference of Φ500 between the regions 55°–65°N, 125°–160°W and 20°–35°N, 125°–160°W. The daily data of the EPO index were obtained from NOAA/Earth System Research Laboratory (https://psl.noaa.gov/data/timeseries/daily/EPO/) and were averaged to monthly values. We obtained all the other climate indices used here from the NOAA Climate Prediction Center (CPC).

We applied empirical orthogonal function (EOF) and singular value decomposition (SVD) analyses to the yearly 2-m air temperature (T_{2m}) and geopotential height at 500 hPa (Φ500), averaged from December to the following February. In the EOF and SVD analyses, we ensured that correlations between different modes were low and insignificant and that these modes were well separated. We calculated the quasi-geostrophic (QG) streamfunction and the wave activity flux (WAF) following Takaya and Nakamura (2001) based on the NCEP Reanalysis II dataset. To ensure the robustness, we repeated the EOF and SVD analyses for two additional atmospheric reanalysis datasets: the fifth generation of atmospheric reanalysis produced by the European Centre for Medium-Range Weather Forecasts (ERA5; Hersbach et al. 2020) and the Modern-Era Retrospective Analysis for Research

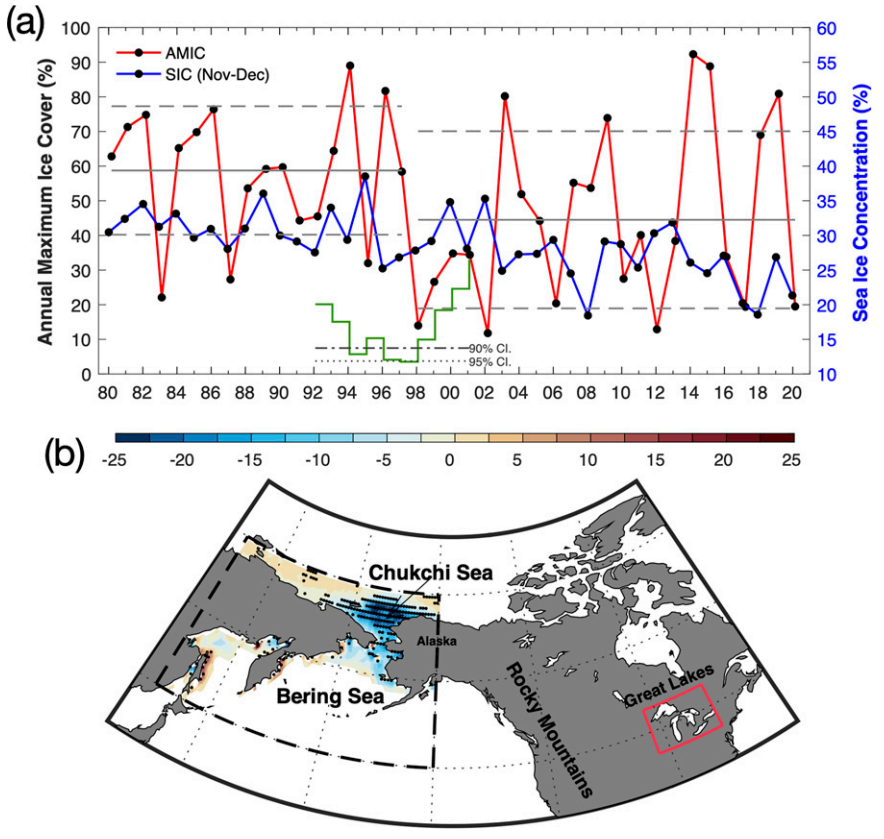

FIG. 1. (a) Annual maximum ice cover (AMIC; %) from 1980 to 2020 (red line with black dots). The blue line with black dots indicates the sea ice concentration (SIC) averaged within November–December over the Bering Sea (black-dashed box in Fig. 1b). Gray solid lines and gray dashed lines indicate the means and standard deviations of AMIC in earlier (1980–97) and later (1998–2020) periods. The green line indicates the *t*-test *p* value of the separation year for periods before and after. Dotted and dotted–dashed lines indicate the 95% and 90% confidence levels, respectively, for determining the step change of AMIC based on the Wilcoxon rank sum test. (b) Sea ice concentration difference between the two periods (later minus earlier period). Dots indicate that the difference between the two periods reaches the 95% confidence level based on the *t* test. The black dashed box indicates the region for calculating the SIC that is shown as a blue line in Fig. 1a. The red box indicates the Great Lakes area for accumulated freezing degree days.

and Applications, version 2 (MERRA-2; Gelaro et al. 2017). The analysis indicated that the spatial resolutions for ERA-5 and MERRA-2 were 0.25° × 0.25° and 0.625° × 0.5°, respectively. Due to computational limitation, we resampled these datasets at 1° × 1° for the SVD analysis.

We applied the two-tailed *t* test, the *F* test, and the Wilcoxon rank sum test (hereafter simply Wilcoxon test; Wilcoxon 1945) here to determine the significant changes in the mean, standard deviation, and step change, respectively, of AMIC and the climate indices. We applied both the *t* test and the Wilcoxon test to identify the significant difference in mean values between the two groups. The Wilcoxon test is a nonparametric test and is more appropriate for data that are not necessarily normally distributed, such as AMIC data (Fig. 1a). The standard for determining the significance in this study is when the *p* value is smaller than 0.05.

3. Decreased AMIC and the increased interannual variability after the winter of 1997/98

a. AMIC trend and interannual variability

The AMIC time series presents notable and large year-to-year fluctuations with a standard deviation of 23% from 1980 to 2020 (Fig. 1a). In this period, the highest AMIC is 93% in 2013/14, and the lowest AMIC is 12% in 2001/02. The trend of AMIC is significantly negative (-4.7% decade^{-1}, $p < 0.05$) in 1980–2020.

The outcomes of both the *t* test and Wilcoxon test reveal significant changes ($p < 0.05$) of the AMIC in the winter of 1997/98. That winter coincides with one of the largest ENSO events of the twentieth century. The mean ± standard deviation for AMIC is 59% ± 18% and 43% ± 25% before and after the winter of 1997/98, respectively. This decrease in the

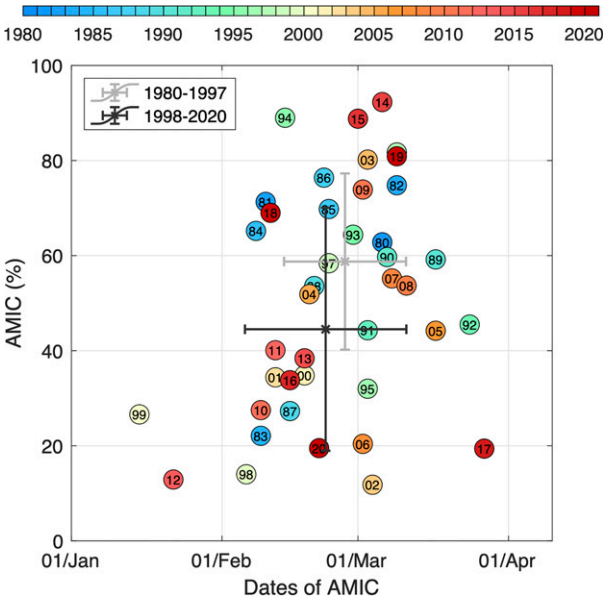

FIG. 2. Scatterplot of dates of AMIC vs AMIC from 1980 to 2020. Crosses indicate the mean and error bars are the standard deviation for dates of AMIC (horizontal) and AMIC (vertical) of earlier (gray) and later (black) periods.

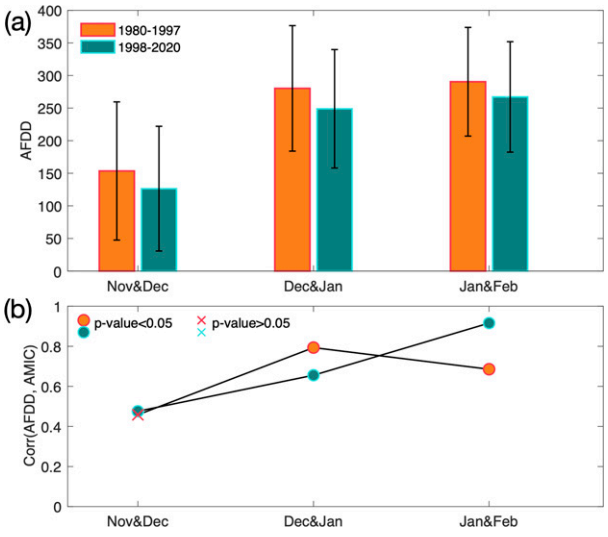

FIG. 3. (a) Accumulated freezing degree days (AFDDs) in November–December, December–January, and January–February of the periods before (1980–97; orange) and after (1998–2020; green) the winter of 1997/98 over the area of the Great Lakes (red box in Fig. 1b). Standard deviations are marked as black bars. (b) Correlations between the AFDDs in November–December, December–January, and January–February and AMIC of the periods before (1980–97; orange) and after (1998–2020; green) the winter of 1997/98. Circle and cross symbols indicate the p values of the correlation coefficient.

mean AMIC is consistent with the previous study on the evaporation rate, the summer water temperature, and the ice cover of Lake Superior (Van Cleave et al. 2014), which accounts for the largest portion of the Great Lakes. In addition, the step change in the winter 1997/98 matches with the turning points of the winter conditions over the midlatitude in the Northern Hemisphere reported by Cohen et al. (2014). The increased standard deviation after the 1997/98 winter represents the increased interannual variability. The extremely high/low AMICs that occurred after the late 1990s, including the highest (2013/14) and the lowest (2001/02) AMIC events (Fig. 1a), also reflect this higher variability. In the following analyses, the AMIC and the related dominating factors are separated into periods of 1980–97 and 1998–2020 based on this step change in the winter of 1997/98. The results are compared between the two periods, as well as with those over the entire period of the dataset (1980–2020).

The dates of AMIC occurrence between 1980 and 2020 are primarily spread between February and early March (Fig. 2). The average date of AMIC occurrence from 1980 to 2020 is on February 24 with a standard deviation of 15 days. After the winter of 1997/98, the date of AMIC occurrence and AMIC itself show a larger spread (Fig. 2). The standard deviation of the date of AMIC occurrence is 12 days in 1980–97, and it jump to 17 days in 1998–2020. In addition to the significant difference of mean AMIC between the two periods, the frequency of larger AMICs (AMIC $>$ 50%) also decreased greatly from nearly three-quarters in 1980–97 to about one-quarter in 1998–2020. Even so, some of the AMICs remained high in the later period (e.g., 2013/14, 2014/15), which is the cause for the higher standard deviation shown in 1998–2020.

Interestingly, this separation in the winter of 1997/98 is also observed in sea ice concentration (SIC) over the Bering and Chukchi Seas. SIC in November–December (SIC_{ND}) decreased by average of 25% after the winter of 1997/98 (Fig. 1b). The negative trend of SIC_{ND} is accelerated from an insignificant rate of −1.7% per decade in 1980–97 to a significant rate of −3.7% ($p < 0.05$) per decade in 1998–2020 (Fig. 1a; Cai et al. 2021). In general, the SIC_{ND} in the Bering–Chukchi Seas revealed an opposite fluctuation to AMIC during 1998–2020. Direct correlation between AMIC and SIC_{ND} is increased from 0.12 in 1980–97 to 0.33 in 1998–2020, although both are insignificant. These changes in AMIC and SIC_{ND} indicate alternatives in large-scale atmospheric patterns after the winter of 1997/98, which impacted ice cover in the two distant locations.

b. *Changes in the winter severity represented in AFDD*

Figure 3 shows the AFDDs in the two-month periods (November–December, December–January, and January–February) prior to the AMIC occurrence over the Great Lakes area (red box of Fig. 1b). From 1980–97 to 1998–2020, the two-month AFDDs decreased by 18%, 11%, and 8% in November–December, December–January, and January–February, respectively. On the other hand, the analysis shows that the standard deviations were similar in the two periods with a difference less than 10% (Fig. 3a). The difference of AFDDs in November–December between 1980–97 and 1998–2020 reaches the 90% confidence level based on a t test. No significant change of variation (F test) and step changes

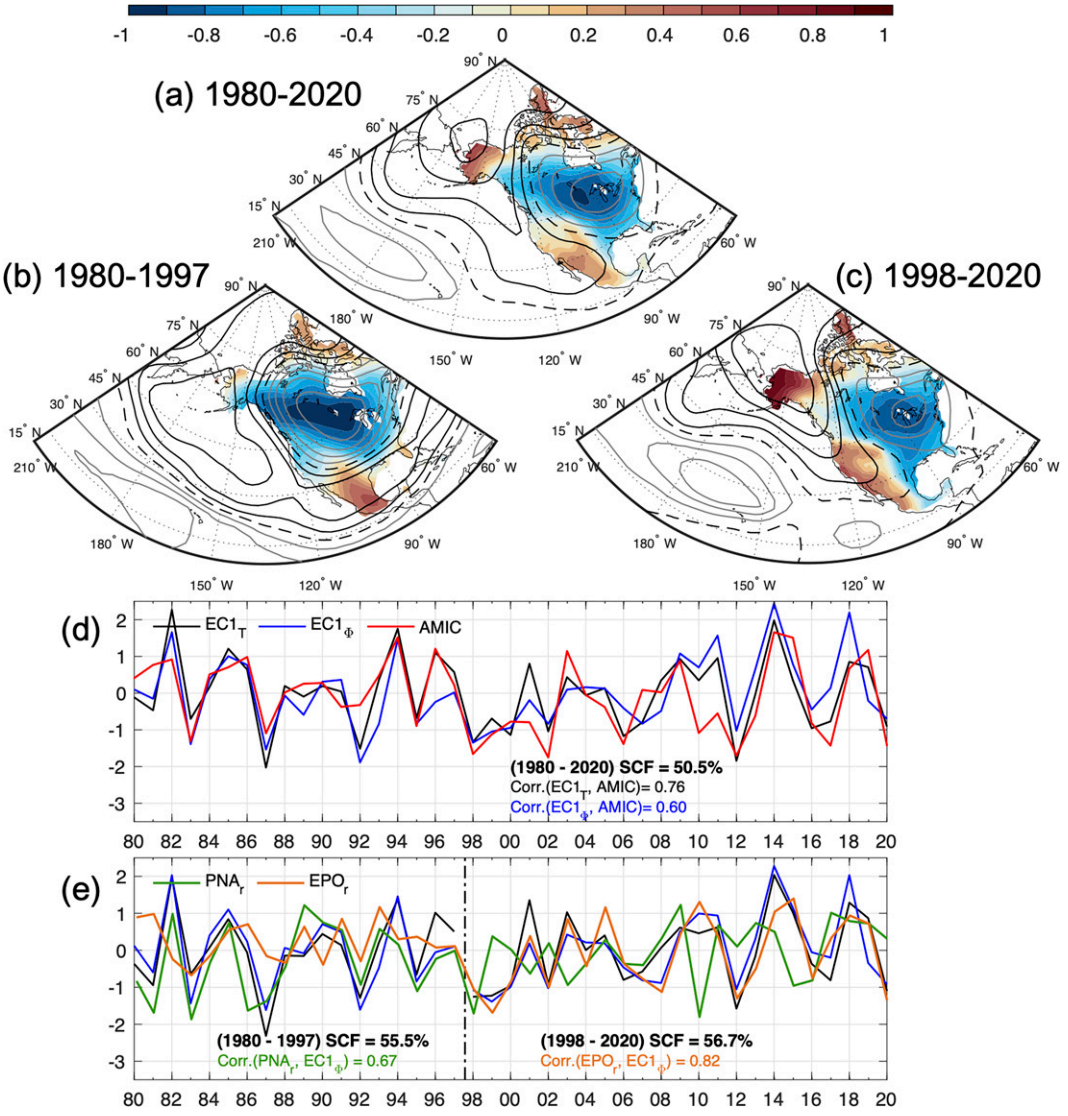

FIG. 4. Spatial patterns of SVD modes 1 for T_{2m} (color) and Φ500 (contour) averaged over December to February of (a) 1980–2020, (b) 1980–97, and (c) 1998–2020. Expansion coefficients of T_{2m} ($EC1_{T2m}$; black) and Φ500 ($EC1\Phi_{500}$; blue) of (d) 1980–2020 and (e) 1980–97 (years before vertical dashed line) and 1998–2020 (years after vertical dashed line). All expansion coefficients are normalized by their respective standard deviations. The vertical dashed line in (e) indicates the year of 1997 for separation. SCF is the square covariance fraction, and r is the correlation coefficient between the two expansion coefficients. The red line in (d) is the AMIC, the green line in (e) is the PNA_r, and the orange line in (e) is the EPO_r, where the subscript r indicates the reversed index. Both AMIC and EPO are normalized by their standard deviations, except for PNA. Corr(A, B) denotes the correlation coefficient between A and B. All Corr(A, B) listed here reach the 95% confidence level.

(Wilcoxon test) was found in the other two-month periods (December–January or January–February).

Figure 3b shows the correlations between the two-month AFDDs and the corresponding AMIC during 1980–97 and 1998–2020. In both periods, AMIC and AFDDs are significantly correlated with high values in December–January and January–February. The highest correlation is changed from December–January (r = 0.81) in 1980–97 to January–February (r = 0.94) in 1998–2020. This may indicate that Great Lakes ice cover is more sensitive to cold episodes later in the season (January and February) in 1998–2020.

4. Atmospheric circulation patterns related with AMIC and their changes after the winter of 1997/98

a. *Covarying mode of Φ500 and T_{2m}*

Figure 4 shows the SVD mode 1 of Φ500 and T_{2m} in 1980–2020, 1980–97, and 1998–2020. The SVD mode 1 in

TABLE 1. Correlation coefficient between AMIC and monthly climate indices averaged over DJF in the earlier (1980–97) and later (1998–2020) periods and in the entire period (1980–2020). Numbers in bold indicate the correlation coefficients reached the 95% confidence level.

	ENSO	PDO	NAO	AO	PNA	TNH	EPO
AMIC (1980–97)	**−0.65**	0.03	**−0.55**	−0.35	**−0.48**	0.28	−0.38
AMIC (1998–2020)	0.01	0.22	0.06	0.06	−0.17	**0.60**	**−0.63**
AMIC (1980–2020)	−0.17	0.26	−0.18	−0.09	−0.25	**0.43**	**−0.58**

1980–2020 has a squared covariance fraction (SCF) of 50%, which accounts for about half of the total variance (Fig. 4a). Spatial pattern 1 (sp1) of T_{2m} reveals a negative center over North America, including the region west of the Great Lakes, and had positive anomalies over Alaska, the southwest coast of the United States, and the Canadian Arctic Archipelago (CAA), which coincides with the features of warm Arctic and cold continents (Overland et al. 2011; Cohen et al. 2014; Kug et al. 2015; Blackport et al. 2019; Guan et al. 2021). The sp1 of Φ500 shows a dipole structure, with the negative center over central North America and the positive center over the Bering and Chukchi Seas (contours in Fig. 4a). The expansion coefficients (ec1) of T_{2m} and Φ500 are highly correlated with each other ($r = 0.85$). They both also have a significant correlation with AMIC (red line in Fig. 4d), where the $r = 0.7$ ($p < 0.05$) for T_{2m} and $r = 0.6$ ($p < 0.05$) for the Φ500. This is expected given that the dipole pattern in the SVD analysis represents the ridge–trough dipole pattern over North America, which is known to steer cold air masses from the Arctic into central North America (Bai and Wang 2012; Wang et al. 2015). This anomalous circulation is reversed during low AMIC years.

The SVD modes 1 in 1980–97 and 1998–2020 account for 55.5% and 52.6% of their total variances, respectively. Similar to the entire period (1980–2020), the sp1 of T_{2m} in both periods have a minimum west of the Great Lakes, and the sp1 of Φ500 shows a dipole structure over the North Pacific and North America. After the winter of 1997/98, however, the SVD modes 1 of T_{2m} and Φ500 present a notable change. The sp1 of T_{2m} in 1998–2020 has a weakened negative center over the area west of the Great Lakes compared to the earlier period (Figs. 4b,c). Most notably, the dipole structure of the sp1 of Φ500 shifts its center northeastward to Alaska, and the Chukchi Sea with a boundary along the Rocky Mountains (Figs. 4b,c).

This shift in the spatial pattern of SVD mode 1 of Φ500 and T_{2m} in 1998–2020 coincides with the changes in the teleconnection patterns that have high correlations with the expansion coefficients. The sp1 of Φ500 in the earlier period shows a negative PNA-like pattern with positive values over the North Pacific and negative in North America (Fig. 4b). The ec1 of Φ500 in 1980–98 has significant correlation coefficients ($r = 0.67$, $p < 0.05$) with the inverted (i.e., multiplied by −1) PNA index (Fig. 4e). The inverted climate indices here mean "multiplied by −1." As the dipole structure is shifted northeastward during 1998–2020, the ec1 of Φ500 becomes highly correlated to the EPO index ($r = 0.82$, $p < 0.05$; Fig. 4e), but is insignificantly correlated with the PNA index. Similar results are found in the SVD analyses using a few other reanalysis products of ERA5 and MERRA-2 (Fig. A1 in the appendix).

b. Correlations with climate indices

Table 1 shows the correlations between AMIC and multiple climate indices averaged in December–February. During 1980–97, the AMIC is significantly correlated ($p < 0.05$) with the climate indices of ENSO, NAO, and PNA with correlation coefficients $r = -0.65$, -0.55, and -0.48, respectively. This is somewhat consistent with Bai et al. (2012) and Wang et al. (2018), who suggested there were combination effects from multiple teleconnection patterns on the Great Lakes regional weather. None of these climate indices correlated with AMIC in 1998–2020, after the winter of 1997/98. We also examine the regression of Φ500 onto the ENSO, as well as the NAO and the PNA in both periods (not shown); the patterns are similar in the two periods. It is unlikely that these teleconnection patterns had rapidly changed to alter the large changes of correlations between AMIC and ENSO, NAO, and PNA in the two periods (Table 1).

During 1998–2020, AMIC shows high and significant correlations with the TNH ($r = 0.60$, $p < 0.05$) and EPO indices ($r = -0.63$, $p < 0.05$). The positive TNH pattern consists of above-average geopotential heights over the Gulf of Alaska and eastern Gulf of Mexico and below-average height covering northeastern North America. The EPO pattern represents the variability of geopotential height over the Gulf of Alaska and the southeastern subtropical Pacific. The positive phase of the TNH and the negative phase of the EPO result in the ridge of geopotential heights over the Gulf of Alaska because of their centers of action. Given that the ridge steers cold air mass from the Arctic into the Great Lakes region, the correlations of the TNH and EPO indices with AMIC are reasonable. Smith and Sheridan (2021) found that the EPO played a crucial role in the cold air outbreaks over North America, and Marinaro et al. (2015) also found a similar conclusion that the combination of positive TNH and negative EPO affected the severe cold winter of 2013/14 over North America, leading to the second-highest ice cover of the Great Lakes since 1973. However, it is unclear yet why the correlations with the TNH and EPO indices became significant only after the winter of 1997/98.

Figure 5 shows the statistical confidence levels of the *t* test, the *F* test, and the Wilcoxon test for climate indices of ENSO, NAO, AO, PDO, PNA, EPO, and TNH, averaged over December–February, as well as AMIC, to determine the significances of separation years. We tested the separation years from 1990 to 2005. In these three tests, most of the

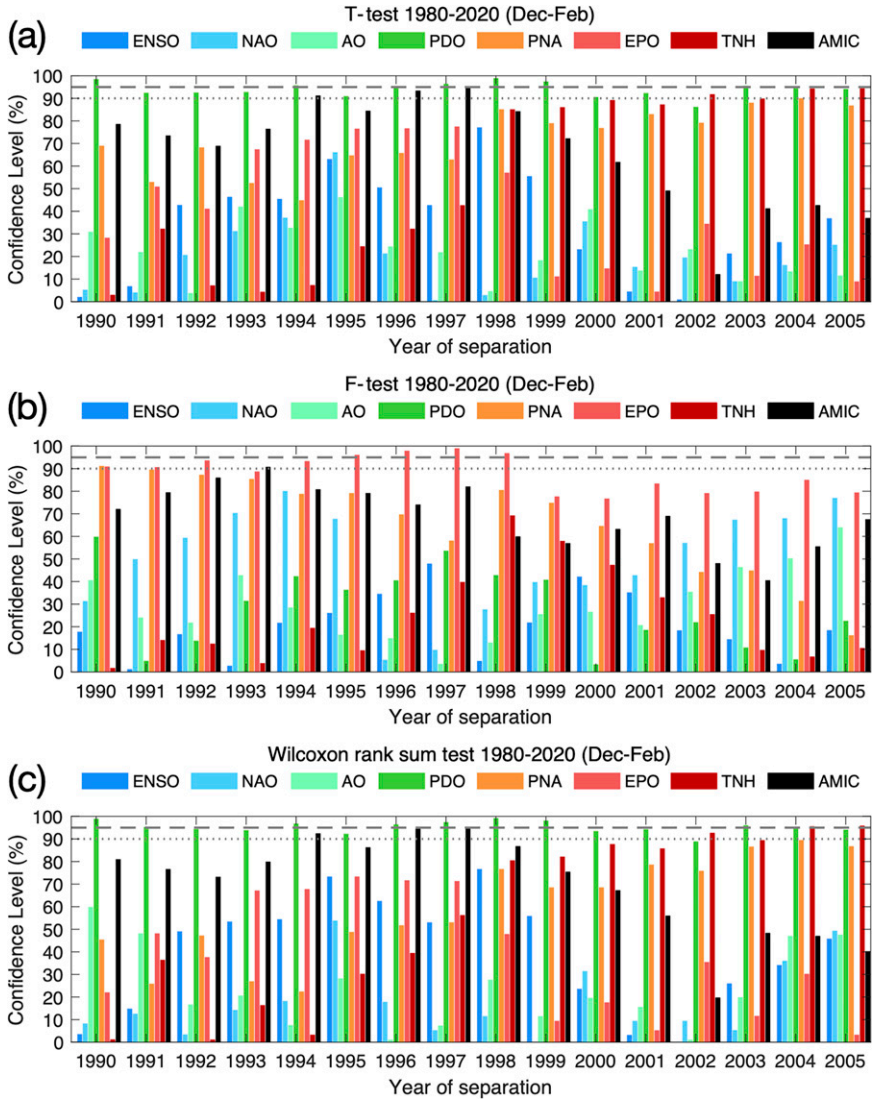

FIG. 5. Confidence levels (%) of the (a) *t* test, (b) *F* test, and (c) Wilcoxon rank sum test on AMIC and multiple climate indices, including ENSO, NAO, AO, PDO, PNA, EPO, and TNH, for determining the significant year of separation between 1990 and 2005. Gray dash-dotted lines indicate the 95% and 90% confidence levels, respectively.

climate indices are not significantly separated from 1990 to 2005 except the PDO and the EPO. The confidence level in the *t* test and Wilcoxon rank sum test is greater than 95% for the PDO index, mainly in 1997–99 in response to its phase change from positive to negative around the late 1990s to earlier 2000s. For the EPO index, the confidence level in the *F* test reached 95% in 1995, gradually increased in the following years, and reached the maximum in 1997/98 (Fig. 5b). The standard deviations of the EPO index are 28.0 in 1980–97 and 52.2 in 1998–2020, suggesting an increasing interannual variability of the EPO index after the winter of 1997/98. This is likely related to the fact that AMIC started to significantly correlate with the EPO index at the same time. Next, we examine the relations of AMIC with large-scale atmospheric patterns.

c. *Correlation of AMIC with 500-hPa geopotential height and surface air temperature*

Figures 6 and 7 show the correlation fields of AMIC with the Φ500, $T_{2m,}$ and SST in December–February and the two-month periods (November–December, December–January, and January–February) prior to the AMIC. The correlation map in December–February before the winter of 1997/98 shows a dipole structure of Φ500, with positive anomalies over Alaska southward toward Texas and northern Mexico and negative anomalies centered over the Great Lakes, showing a negative PNA-like pattern across the North Pacific and North America (Fig. 6a). The AMIC-correlated T_{2m} shows a positive anomaly over the East Siberian Sea, Chukchi Sea,

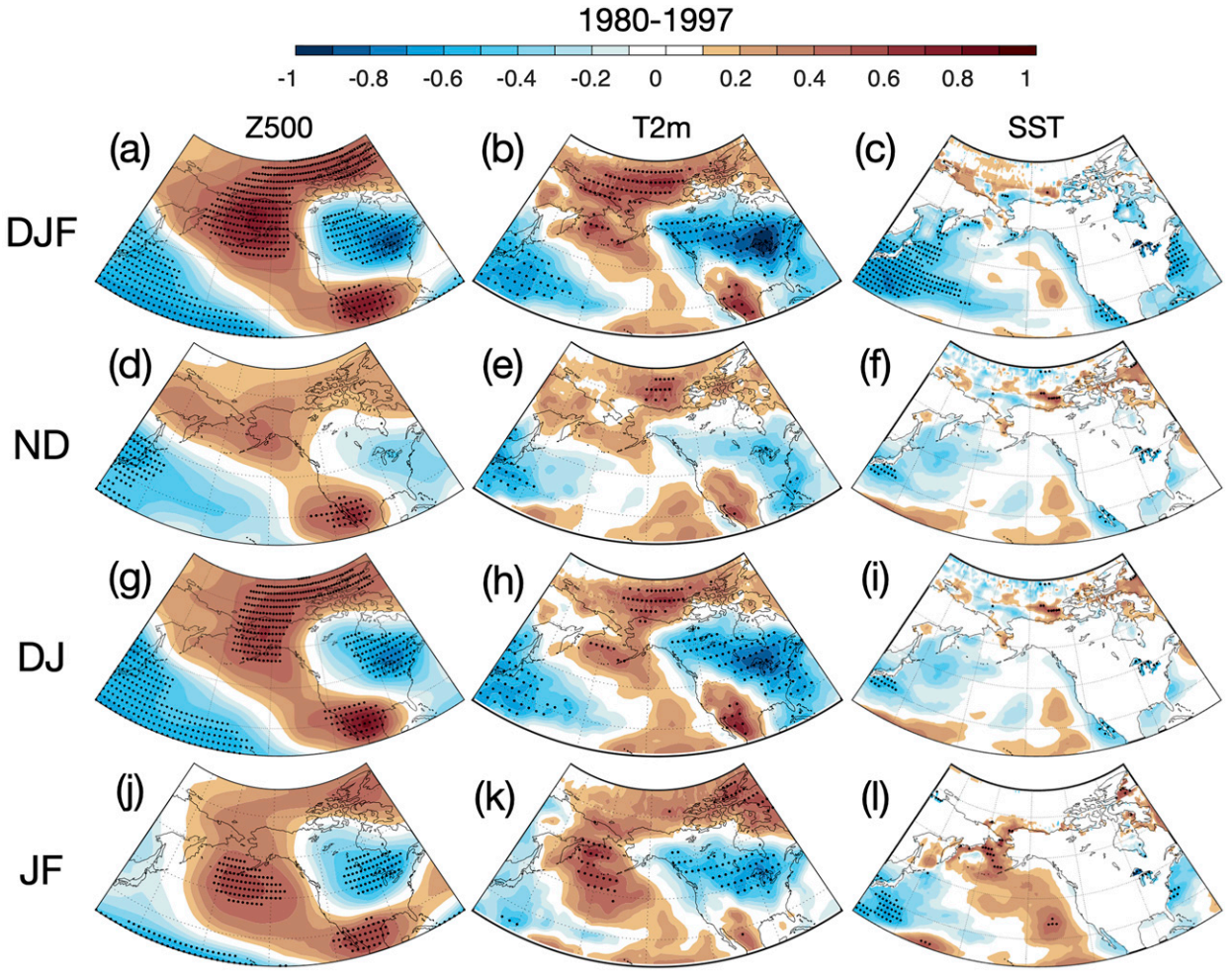

FIG. 6. Correlation maps between AMIC and (left) Φ500, (center) surface air temperature, and (right) sea surface temperature in (a)–(c) December–February (DJF), (d)–(f) November–December (ND), (g)–(i) December–January (DJ), and (j)–(l) January–February (JF) of the period before the step change (1980–97). Dots indicate the correlation reached the 95% confidence level.

and Beaufort Sea and a negative anomaly covering North America before the winter of 1997/98 (Fig. 6b). The distributions of Φ500 and T_{2m} are similar to the SVD results shown in Fig. 4a (i.e., the warm Arctic–cold continent feature). The dipole pattern of AMIC-correlated Φ500 is insignificant in November–December (Fig. 6d) but becomes significant in December–January (Fig. 6g). This dipole pattern moves southward in January–February (Fig. 6j). The AMIC-correlated T_{2m} reflects the negative center over the Great Lakes region (Figs. 6e,h,k), and the correlation map of AMIC and T_{2m} is significant in December–January (Fig. 6h) and January–February (Fig. 6k).

The series of correlation maps from 1998 to 2020 shows a moving dipole pattern (Fig. 7). The correlation map from December to February between AMIC and Φ500 shows a positive anomaly covering Alaska and the northeastern Pacific and a negative anomaly over the eastern North America (Fig. 7a). Notably, the dipole pattern is more condensed over the over the continent of North America in 1998–2020 (Fig. 7a) compared with the 1980–97 result (Fig. 6a), where the positive portion is located at the Alaskan Peninsula. This condensed dipole indicates an eastward movement of the dominant weather pattern, leading to extreme cold or warm winters. Furthermore, the dipole structure developed in November and December, which is earlier than in the period of 1980–97 (Fig. 7d), with positive correlation coefficients over Alaska ($r = 0.65$, $p < 0.05$ at the positive center) and negative correlation over the northern part of the Great Lakes (Fig. 7d). This dipole feature of Φ500 over North America in 1998–2020 persists from November to February (Figs. 7a,d,g,j), and the contrast of the dipole in January and February shown in Fig. 7j is more evident than in 1980–97 (Fig. 6j). This persistent dipole feature in the AMIC–Φ500 correlation map during 1998–2020 indicates that AMIC is likely more sensitive to the ridge–trough system, implying a connection to the jet stream. This conjecture is consistent with the previous studies showing that the frequency of high-amplitude jet stream days has increased since the late 1990s (Francis and Vavrus 2012; Chen et al.

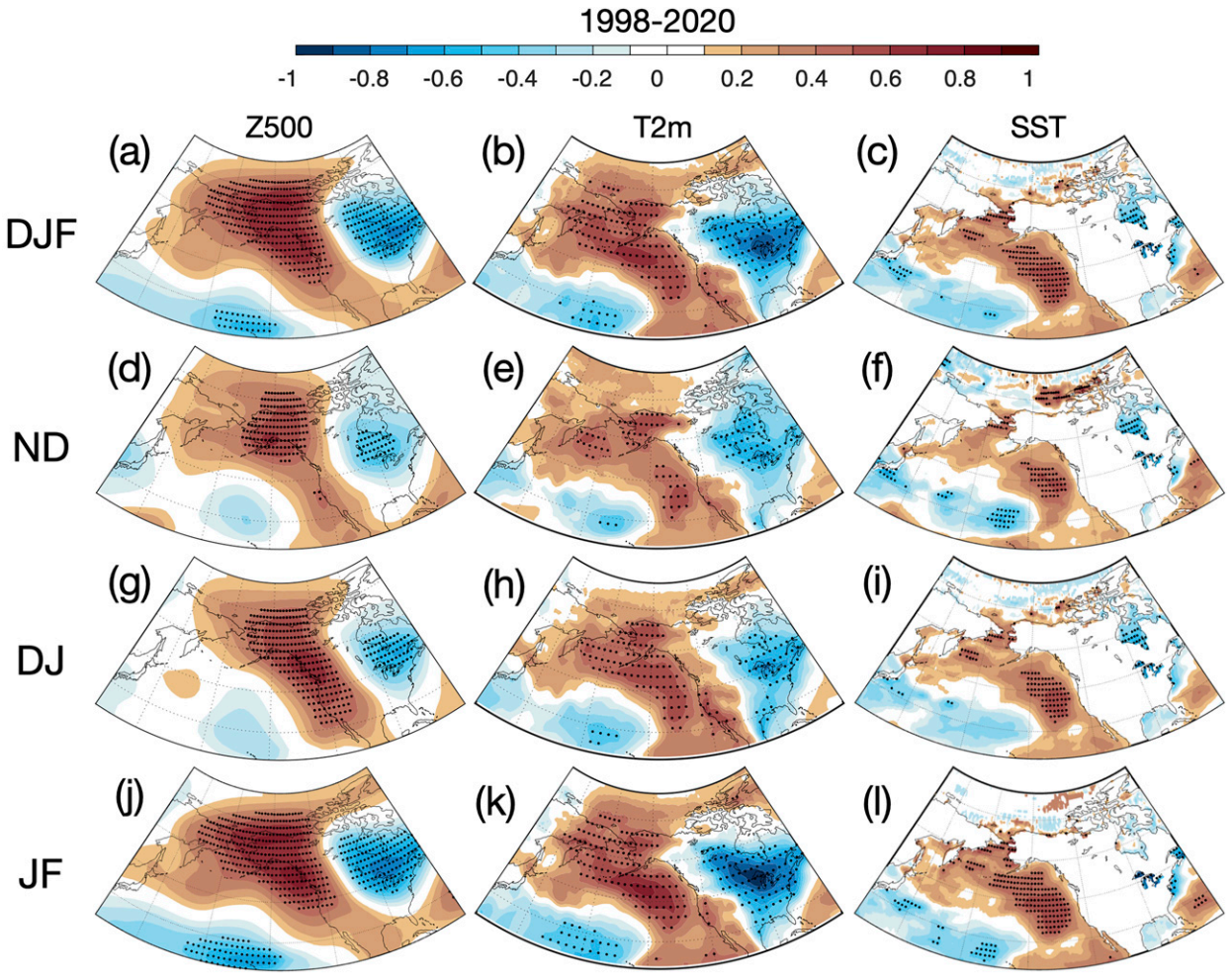

FIG. 7. As in Fig. 6, but for the period after the step change (1998–2020).

2015; Cattiaux et al. 2016; Röthlisberger et al. 2016; Vavrus et al. 2017). One notable feature is that the correlation patterns of both AMIC–Φ500 (Figs. 7a,d,g,j) and AMIC–T_{2m} (Figs. 7b,e,h,k) show no significant correlation over the Arctic Ocean.

The positive anomaly of the dipole pattern in the AMIC–Φ500 correlation maps covering 1998–2020 is located in a similar region to the positive center of TNH and the negative center of EPO in their positive phases (Figs. 7a,d,g,j). The pattern is also consistent with a single Φ500 anomaly of TNH, identified by Liang et al. (2017), which dominated the Gulf of Alaska in the winter season. This amplified atmospheric ridging of positive geopotential height over the greater Alaska area could explain the reduced sea ice in the Chukchi Sea in early winter after the winter of 1997/98 (Overland et al. 2021), in addition to the warming of surface air temperature around the Chukchi Sea (Kug et al. 2015).

Similar to 1980–97, the correlation maps of AMIC–T_{2m} in 1998–2020 show a negative center over the Great Lakes region from November to February (Figs. 7b,e,h,k); however, the strongest correlation appears in January–February (Fig. 7k), after the winter of 1997/98.

d. *Warm blob signal in AMIC–SST correlation in the 1998–2020 period*

The AMIC–SST correlation maps for 1980–97 (Figs. 6c,f,i,l) show a negative anomaly over the northwest Pacific with a small fraction of positive anomaly to the northeast Pacific, weakly following the AMIC-T_{2m} correlation pattern (Figs. 6b,e,h,k). On the other hand, in 1998–2020, data show that a significantly positive anomaly occupied the entire Gulf of Alaska, which corresponds to the "Pacific warm blob" (Bond et al. 2015) throughout November to February (Figs. 7c,f,i,l). The highest correlation between AMIC and SST is r = 0.72 in January–February off the coast of North America. Previous studies have suggested that this Pacific warm blob was formed due to the stronger wind induced by the higher-than-normal atmospheric pressure over the Gulf of Alaska (Bond et al. 2015) and was linked to the teleconnection index TNH with a one-month

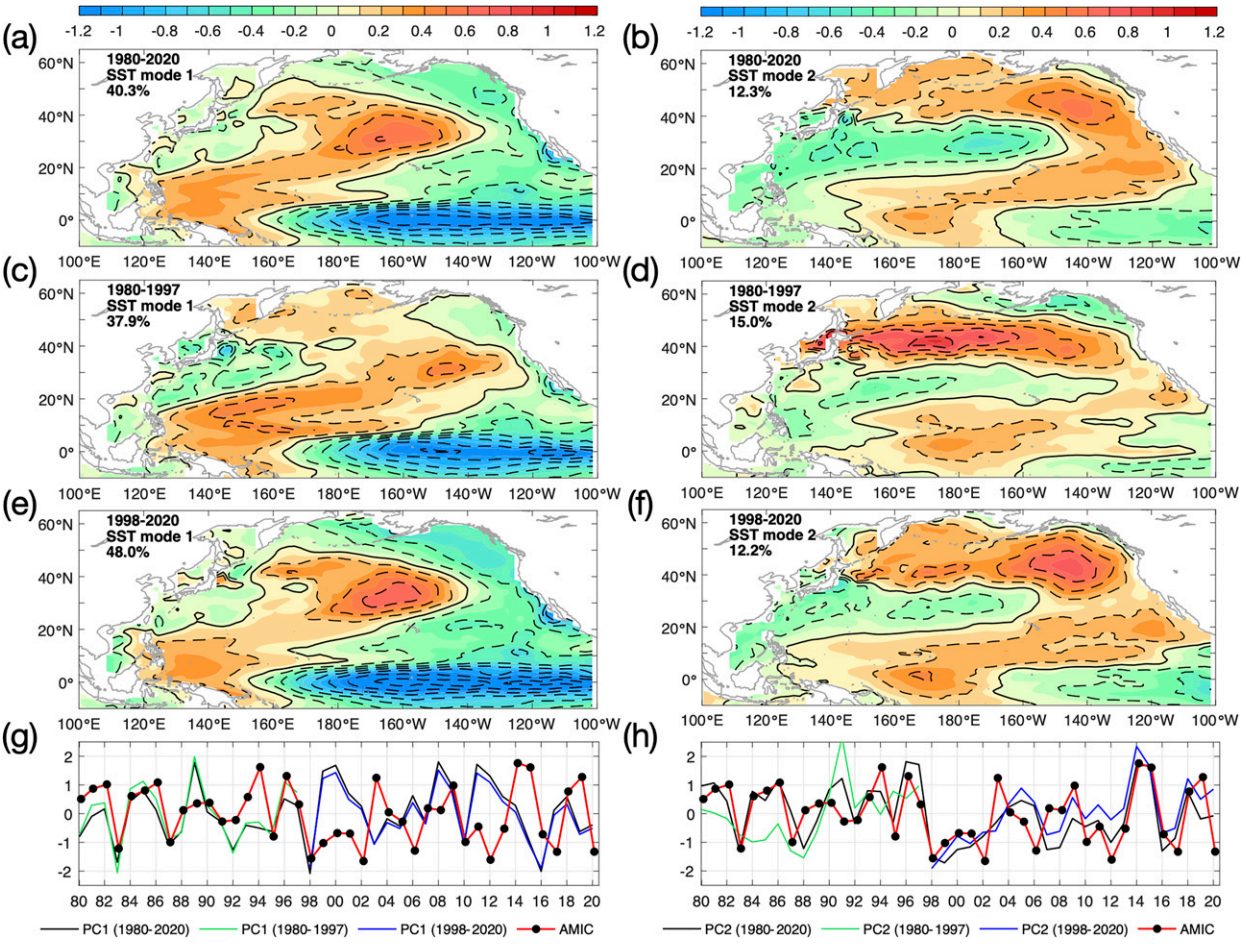

FIG. 8. EOF (a),(c),(e) mode 1 and (b),(d),(f) mode 2 for sea surface temperature (SST) averaged over December–February of (a),(b) 1980–2020, (c),(d) 1980–97, and (e),(f) 1998–2020. Colored maps are eigenvectors (°C). The black solid line indicates the contour at 0. (g),(h) The principal components of modes 1 and 2, respectively. Principal components of EOF in periods of 1980–2020, 1980–97, and 1998–2020 are shown in black, green, and blue in (g) and (h). The red time series with black dots represents the normalized AMIC for comparison with PCs. The pc1 in 1980–97 is significantly correlated with AMIC ($r = 0.63$), and the others are not. The correlations between the pc2 in 1980–2020 and in 1998–2020 and AMIC are 0.62 and 0.66, respectively.

lag time (Liang et al. 2017). In general, the locations of AMIC-correlated patterns of Φ500 and SST are consistent with the Pacific warm blob and TNH presented by Liang et al. (2017). In addition, the positive anomalies of AMIC-correlated T_{2m} and SST in earlier winter (November–December) covers the entire Bering Sea and reached the Chukchi Sea, likely contributing to the reduction of SIC in November–December in 1998–2020 and the delay of sea ice formation (Fig. 1).

5. SST variability over the North Pacific and the stationary Rossby wave propagation

a. *SST variability over the North Pacific*

Figure 8 shows the EOF of SST over the North Pacific from 10°S to 65°N during 1980–2020, 1980–97, and 1998–2020. Mode 1 of 1980–2020, 1980–97, and 1998–2020 accounts for 40%, 38%, and 48% of their total variances (Figs. 8a,c,e), respectively. The eigenvector of mode 1 (ev1) in 1980–2020 reveals a La Niña–like pattern (or negative ENSO) in which the strong negative anomaly extends from the eastern equatorial Pacific with the opposite sign in the central Pacific (Fig. 8a). The ev1 of SST in 1980–2020 and 1998–2020 show larger positive-negative contrast over the central Pacific and eastern equatorial Pacific, but the positive anomaly in 1980–97 is more evident over the western North Pacific (Fig. 8c). The principal component of mode 1 (pc1) in 1980–2020 shows a high correlation with the ENSO index (Fig. 8g), where $r = -0.97$. In addition to ENSO, pc1 in 1980–2020 also shows a significant correlation with PNA ($r = -0.63$, $p < 0.05$), PDO ($r = -0.58$, $p < 0.05$), and TNH ($r = 0.48$, $p < 0.05$) (see Table 2). The pc1 of SST in 1980–97 also has significant correlations with these climate indices, except for PDO. On the other hand, in 1998–2020, the pc1 of SST presents a significant correlation with PDO ($r = -0.78$, $p < 0.05$), instead of TNH (Table 2).

Mode 2 of SST in 1980–2020, 1980–97, and 1998–2020 accounts for 12%, 15%, and 12% of their total variances (Figs. 8b,d,f),

TABLE 2. Correlation coefficient between the principal components of SST EOF modes 1 and 2 (pc1 and pc2; see Fig. 8) and the monthly climate indices averaged over DJF in the earlier (1980–97), the later (1998–2020), and entire (1980–2020) periods. Numbers in bold indicate the correlation coefficients reached the 95% confidence level.

	ENSO	PDO	NAO	AO	PNA	TNH	EPO
pc1 (1980–97)	**−0.98**	−0.02	−0.22	0.06	**−0.58**	**0.62**	−0.38
pc1 (1998–2020)	**−0.98**	**−0.78**	0.04	0.22	**−0.62**	0.37	0.26
pc1 (1980–2020)	**−0.97**	**−0.58**	−0.01	0.20	**−0.63**	**0.48**	−0.13
pc2 (1980–97)	0.04	**−0.68**	0.03	0.22	−0.24	0.05	−0.38
pc2 (1998–2020)	−0.09	−0.03	0.07	0.10	−0.35	**0.53**	**−0.58**
pc2 (1980–2020)	−0.14	0.28	−0.23	−0.12	−0.09	0.24	**−0.62**

respectively. The ev2 in 1980–2020 shows a positive temperature anomaly inside the Gulf of Alaska, and this positive anomaly extends northward into the Bering Sea and southwestward into the subtropical North Pacific (Fig. 8b), which is recognized as the North Pacific mode (Deser and Blackmon 1995; Park et al. 2012; Hartmann 2015). Similar spatial distributions of ev1 and ev2 of the EOF SST were found by Guan et al. (2021) from 1979 to 2013, where the latter was suggested to contribute to the warm Arctic–cold continents pattern over North America. The pc2 of SST EOF in 1980–2020 shows significant correlation only with EPO ($r = 0.62$, $p < 0.05$). The ev2 of SST in 1980–97 reveals a PDO-like structure with negative anomalies extending from east of Japan to the center of the Pacific (Fig. 8d). This is also reflected in the correlation between pc2 in 1980–97 and the PDO ($r = -0.68$, $p < 0.05$). The ev2 of SST in 1998–2020 (Fig. 8f) displays a pattern that is similar to ev2 of 1980–2020 (Fig. 8b), but the contrast of ev1 is enhanced, especially over the Gulf of Alaska in 1998–2020. This positive SST anomaly (ev2) over the Gulf of Alaska is similar to the Pacific warm blob (Bond et al. 2015), which is identified as the major phenomenon influencing the atmospheric circulation above the Alaska area (Liang et al. 2017). The pc2 in 1998–2020 is negative and reveals low variability in the late 1990s and early 2000s, and its fluctuation became large in the late 2010s, coinciding with the recent increase in the interannual variability of AMIC. The pc2 in 1998–2020 shows significant correlations with EPO ($r = -0.58$, $p < 0.05$) and TNH ($r = 0.53$, $p < 0.05$) and is not correlated with other climate indices, also indicating the dominant teleconnection patterns of the Alaska area that is associated with the SST variability over the northeastern Pacific.

The winter of 1997/98 coincided with the shift in PDO from the positive phase to the negative phase. The interdecadal variability of SST over the tropical and North Pacific has been extensively studied since the initial descriptions by Zhang et al. (1997), Mantua et al. (1997), Gershunov and Barnett (1998), and Power et al. (1998). Although the leading mode resembles the sign reversal PDO feature throughout the periods (Figs. 8a,c,e), the change in the second mode of SST EOF after the 1997/98 winter is possibly associated with this PDO phase change (Zhang et al. 1997; Ding et al. 2013). Di Lorenzo et al. (2008) reported that the second mode of EOF of the sea level anomaly over the North Pacific, which was defined as the North Pacific Gyre Oscillation (NPGO), was frequently positive and peaked around the year 2000 after this PDO phase change. Both the positive PDO and NPGO were found to be tied separately to the atmospheric cyclonic circulations mainly located in the Gulf of Alaska (Chhak et al. 2009), where the former is linked to the overlying Aleutian low and the latter is forced by the North Pacific Oscillation (NPO). Their suggested mechanism is similar to the findings of atmospheric controls on northeast Pacific SST (Johnstone and Mantua 2014; Bond et al. 2015). The interaction of these two atmospheric circulations could lead to increased chances of meandering airflow (e.g., the ridge–trough system; Linkin and Nigam 2008). This appears to be consistent with the sign change in our pc2 after the 1997/98 winter [black line in Fig. 8h; note that the sign is reversed from that in Di Lorenzo et al. (2008)]; however, this is not always the case, and exceptions occur in 2004–05, 2014–15, and 2018. The correlations of pc2 with EPO and TNH after the winter of 1997/98 are likely associated with the phase change in NPGO, and the amplitude is also increased visually after the 1990s compared to the period in the 1980s (see Fig. 3d of Di Lorenzo et al. 2008). Given the spatial pattern of mode 2 (Fig. 8f), pc2 is indeed correlated with the TNH and EPO indices (Table 2), as the positive anomaly over the Gulf of Alaska in mode 2 (Fig. 8f) overlaps with the anomaly areas of TNH and EPO patterns. It is worth noting that the amplitude of EPO index increased after 1998, which might be related to the SST variability over the Gulf of Alaska.

b. *Stationary Rossby wave propagation associated with SST variability*

Figure 9 shows the regressions of the horizontal QG streamfunction and the WAF onto the EOF SST pc1 and pc2 in the three periods. The values are averaged temporally over the winter months (December, January, and February) and vertically for 100–250 hPa. During 1980–2020, analysis of the regression of QG streamfunction onto the SST pc1 reveals a dipole pattern over central North Pacific and northern North America, indicating the long-term contribution of the La Niña–like SST from the North Pacific (Fig. 9a). A small, significant, and positive QG streamfunction anomaly located in southern North America is weakly connected with a major feature in the central North Pacific. A group of WAF is located at the northern edge of the positive anomaly in the central North Pacific pointed northeastward across Alaska into North America (Fig. 9a), indicating propagation of stationary Rossby waves. The contrast of

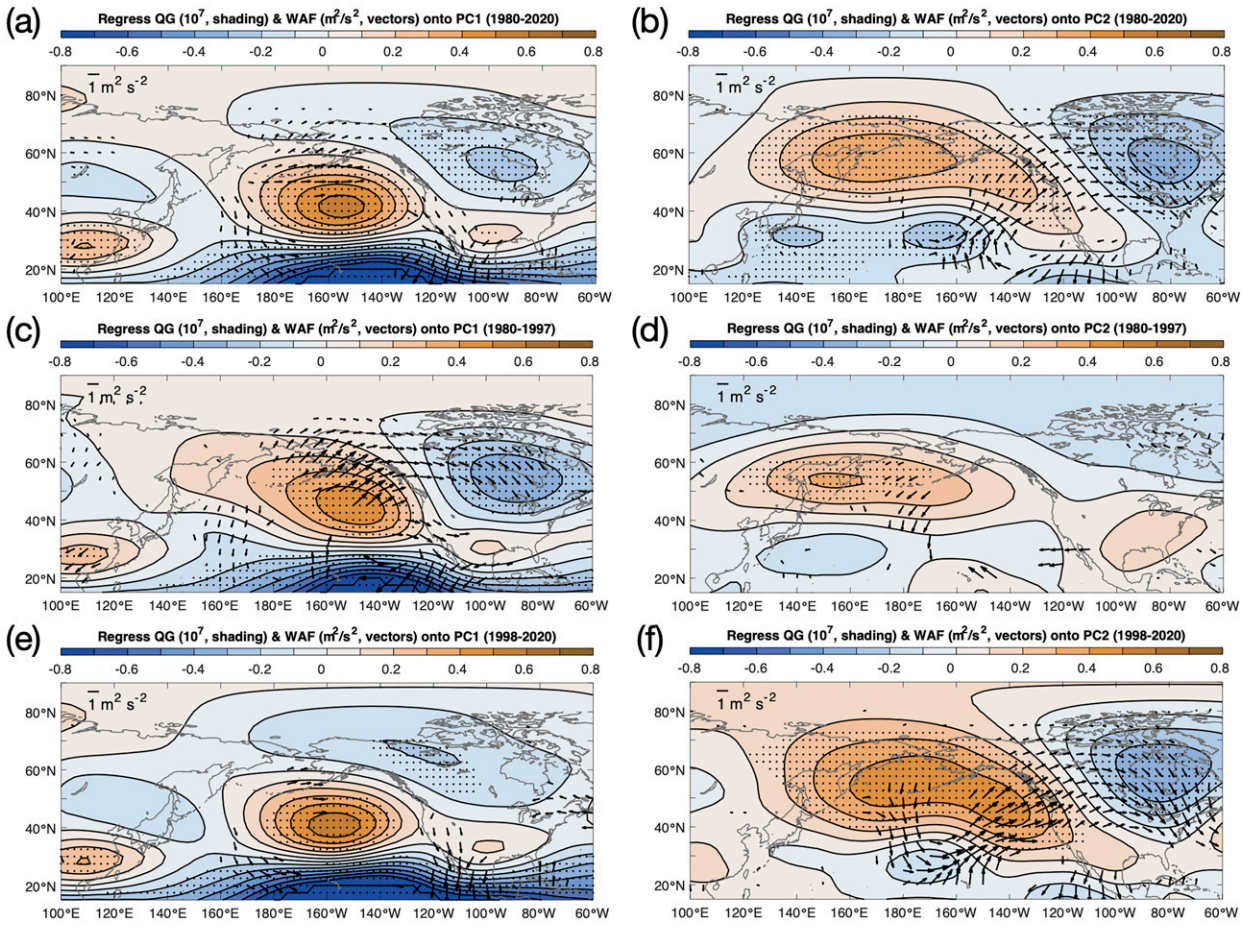

FIG. 9. Quasigeostrophic (QG) streamfunction (10^7; shading; dotted areas for 95% significant level) and wave activity flux (m^2 s^{-2}; vector; black for 90% significant level) in December–February that regresses onto the principal component of the (left) first mode and (right) second mode of SST EOF of (a),(b) 1980–2020, (c),(d) 1980–97, and (e),(f) 1998–2020. The values were averaged over 100–250 hPa. The QG and WAF were calculated following Takaya and Nakamura (2001).

the QG streamfunction dipole and the northeastward WAF is stronger in the regression map of SST pc1 in 1980–97 (Fig. 9c) than in the regression map of SST pc1 in 1998–2020 (Fig. 9e). The regression of WAF onto the SST pc1 in 1980–97 largely covers Alaska and northeastern North America and the regressed WAF arrows point to the downstream areas where the QG streamfunction is negative, suggesting the impacts of SST from the western tropical Pacific on the ridge–trough system over North America before the winter of 1997/98. Such a pattern does not exist in the WAF regression to pc1 in 1998–2020 (Fig. 9e). As shown in the eigenvectors of mode 1 in 1980–97 and 1998–2020 (Figs. 9c,e), the positive anomaly in 1998–2020 shifts southward to cover the central North Pacific whereas in 1980–97 it dominates a larger area over the North Pacific.

The regressions of QG streamfunction and WAF onto the SST pc2 show notable differences in the three periods (Figs. 9b,d,f). Analysis of the regressed QG onto pc2 in 1980–2020 shows a dipole structure along 60°N covering from the western Bering Sea toward the Hudson Bay of northeastern Canada (Fig. 9b). The WAF is sourced from the subtropics points northeastward above the Gulf of Alaska and is connected downstream to eastern North America (Fig. 9b), suggesting a stationary Rossby wave train formed from the northeastern Pacific. The regressed QG streamfunction onto pc2 in 1980–97 reveals a positive center over the Sea of Okhotsk, and the regressed WAF is weaker overall, with the southwestward signal in the south of the Bering Sea (Fig. 9d). The regression of QG streamfunction onto pc2 in 1998–2020 (Fig. 9f) reveals a similar dipole to the period in 1980–2020 (Fig. 9b) but with stronger contrast (Fig. 9f). The differences of the regressed WAF over the Gulf of Alaska reveal that the dominating feature of the SST EOF mode 2 (Fig. 8f) play an import role in forming the ridge–trough system.

Figure 10 shows the pressure–longitude cross section of the regressions of the geopotential height and the WAF onto pc1 and pc2 in 1980–97 (Figs. 10a,b) and in 1998–2020 (Figs. 10c,d). The values were meridionally averaged along the northern edge of the dipole structure (45°–60°N) in December, January, and February. The regressed geopotential height in 1980–97 reveals a positive anomaly centered in the upper troposphere (~200 hPa)

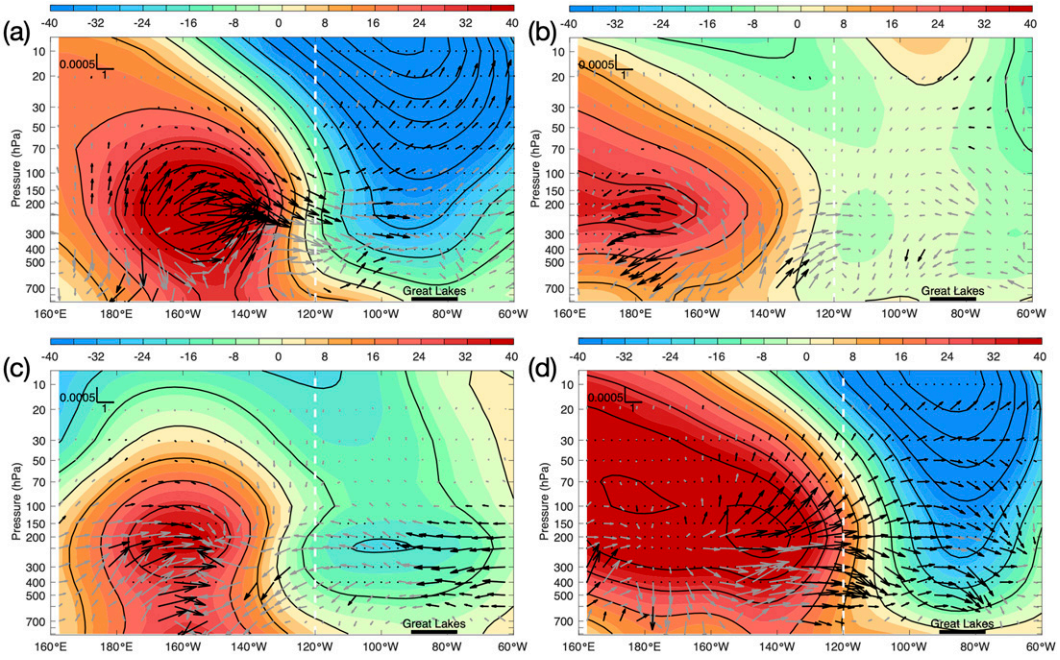

FIG. 10. Pressure–longitude cross section of winter (December–February) geopotential height (m; shading; dotted areas for the 95% confidence level) and wave activity flux ($m^2\ s^{-2}$; vector; black for the 90% confidence level and gray for the rest) that regresses onto the principal component of (a) the first mode of SST EOF in 1980–97, (b) the second mode in 1980–97, (c) the first mode in 1998–2020, and (d) the second mode in 1998–2020. The values were meridionally averaged between 45° and 60°N. The white dashed line indicates the longitude of west coast of North America.

between 130° and 180°W and a negative anomaly extended from the upper stratosphere (~10 hPa) to the lower troposphere (~700 hPa) east of 120°W (Fig. 10a). The regressed WAF in 1980–97 shows that a group of significant WAF is convergent around 140°W and 200 hPa, to the east of the positive anomaly of the regressed geopotential height, indicating stationary Rossby wave propagation off the western coast of North America. Analysis of the regressed geopotential height onto pc2 in 1998–2020 shows that the positive anomaly expands to the west of the date line and the positive center shifts eastward, with a negative anomaly over the Great Lakes area. (Fig. 10d). These patterns disappear in the regressed maps of geopotential height and WAF based on pc2 in 1980–97 (Fig. 10b). Analysis of the regressed WAF onto pc2 shows a clear and significant direction toward downstream dominating the middle and upper troposphere (500 to 150 hPa in Fig. 10d) from 140° to 70°W, where the Great Lakes are located. Moreover, the vertical component of the regressed WAF reveals a downward direction above the Great Lakes region and eastern North America.

c. *Dynamical connection between SST variability and AMIC*

The above analyses support that the SST variability over the North Pacific is strongly connected to the ridge–trough system as well as winter weather over North America, specifically the Great Lakes. As shown in the WAF field (Fig. 9), the stationary Rossby wave propagates eastward across the dipole structure of the regressed QG streamfunctions (and that of geopotential heights) in the northeast Pacific. The notable changes in the SST EOF modes 1 and 2 after the winter of 1997/98 (Figs. 8c,e,d,f) appear to alter the primary source location of the WAF (Fig. 9), whose signal reached up to the stratosphere (Fig. 10). Alongside the results presented in sections 3 and 4, the connection between AMIC and the positive SST anomaly over the northeast Pacific (or the Pacific warm blob) in the 1998–2020 period (Fig. 7) can be explained as follows: The stationary Rossby wave initiated from the warm SST anomaly in the northeast Pacific reaches up to the stratosphere and disrupts the polar vortex, which subsequently altered the tropospheric jet stream. This pathway ultimately shifts the ridge–trough system over North America eastward, covering the Great Lakes region in the trough and impacting AMIC. Considering the tropospheric pathway, this proposed mechanism is consistent with the previous studies. For example, the Pacific warm blob was reported to have positive feedback on the above geopotential height (Hartmann 2015; Liang et al. 2017) and was used to explain the extremely cold winter of North America in 2013/14 (Hartmann 2015; Wang et al. 2014; Lee et al. 2015). Not many studies have examined the connection of the northeast Pacific SST variability with the stratosphere, but Kretschmer et al. (2018) showed two dominant patterns of increased polar cap heights in the lower stratosphere that could impact cold spells over northern Eurasia, central Canada, and the Great Lakes region, which were associated with sudden stratospheric warmings classified by Kodera et al. (2015). Meanwhile, Zhang et al. (2018) presented a stratospheric pathway that connected the cold Siberia pattern in the winter following sea ice loss over the Barents–Kara Seas in late

autumn. For a similar stratospheric pathway that connects the blob-like feature over the northeast Pacific and the cold spell over the Great Lakes, however, more numerical and analytical studies are required.

Why are the SST variability changes and the associated shifts in the atmospheric patterns observed before and after the winter of 1997/98? We did not find a clear answer to this. However, it is very likely that this might involve climate variability in the tropical Pacific. It has been shown that the SST variability over the northeast Pacific is controlled by atmospheric forcing (Johnstone and Mantua 2014; Chhak et al. 2009; Furtado et al. 2012), particularly the NPO, which points to the same pattern as the EPO but has a slightly different definition. The NPO was shown to be a possible mechanism linking the extratropical atmospheric variability to El Niño events in the tropical Pacific (Furtado et al. 2012; Di Lorenzo et al. 2015). Di Lorenzo et al. (2015) combined observational data analysis and coupled ocean–atmosphere modeling experiments to examine the roles of the Pacific meridional mode and ENSO on the low-frequency pattern of the basin-scale SST over the Pacific.

The occurrence of the Pacific warm blob, which was first observed in 2013 (Bond et al. 2015) and has been reported at irregular intervals, may be another manifestation of these changes. However, the forcing mechanism of the blob occurrence is not well understood, including how it interacts with the PDO, the NPGO, or the tropical Pacific. Even though the cause of the changes in the winter of 1997/98 (or possibly in the vicinity) is yet to be investigated, we found a clear connection between AMIC and the SST variability over the Gulf of Alaska after the winter of 1997/98, as well as the suggested dynamical connection of the upward and downstream WAF identified as an intermediary.

6. Summary

Based on the above investigations, we have drawn the following conclusions:

1) The Great Lakes ice cover experienced a significant step-change decrease in its annual maximum ice cover (AMIC) in the winter of 1997/98, which coincides with one of the largest ENSO events in the twentieth century. Simultaneously, the interannual variability of AMIC has increased in the recent two decades. After the winter of 1997/98, the winter severity over the Great Lakes region represented by accumulated freezing degree days (AFDDs) is reduced throughout the winter months. The AMIC is significantly correlated with ENSO, the NAO, and the PNA before the winter of 1997/98, but after that none of these climate indices presents a significant correlation with AMIC. Instead, the TNH and the EPO indices reveal significant correlations with AMIC after the winter of 1997/98, with the former positively and the latter negatively correlated with AMIC.
2) The leading modes of SVD analysis of the Φ500 and the T_{2m} reveal major atmospheric dipole circulation related to the surface air temperature anomalies over North America including the Great Lakes region. Moreover, the results show that the dipole shifts northward to Alaska after the step change in the winter of 1997/98. The correlation map of AMIC with SST over the North Pacific reveals a positive center over the Gulf of Alaska, which was similar to "the Pacific warm blob" after the step change in the winter of 1997/98.
3) An EOF analysis of SST over the North Pacific reveals notable changes between the two periods (1980–97 and 1998–2020), particularly in the second mode, where the blob-like feature is evident in the 1998–2020 period over the Gulf of Alaska, which likely contributed to the formation of "warm Arctic–cold continents" of North America (Guan et al. 2021). The QG streamfunction and wave activity fluxes (WAF), when regressed onto the principal components of the SST EOFs, suggest that the warm SST anomaly over the Gulf of Alaska initiates the upward and downstream propagation of a stationary Rossby wave after the winter of 1997/98, which propagates across the west coast of North America. The regressed WAF signal reaches the upper troposphere and stratosphere, suggesting that the stratosphere pathway whereby the polar vortex is disrupted and is mirrored by the polar jet stream underneath resulted in the amplified ridge–trough system over North America and, therefore, the winter weather over the Great Lakes region.

Although we found a clear connection between the SST variability over the Gulf of Alaska (i.e., the blob-like feature) and AMIC after the winter of 1997/98, as well as the possible dynamical intermediary of the WAF reaching up to the stratosphere, we did not find the reason why the SST variability and associated atmospheric circulations changed after the winter of 1997/98. This change is likely connected to the phase changes of the PDO and the NPGO (the second mode of sea surface height anomaly over the North Pacific), which are themselves driven by the Aleutian low and the NPO, respectively. Previous studies showed that the longer-scale variabilities of the NPGO and the NPO were associated with variability in central tropical Pacific SSTs (Furtado et al. 2012; Di Lorenzo et al. 2015). Thus, it is possible that the changes of AMIC after the winter of 1997/98 may have origins in the tropical Pacific. This warrants further numerical and analytical investigations to fully understand the climate variability over the North Pacific and the Great Lakes region.

Finally, one of the most important topics for the Great Lakes community is the seasonal forecasting of AMIC and the winter severity over the region. Advanced understanding of how the Great Lakes winter climate connects to the larger atmospheric patterns, including the identified connection to the SST anomaly over the Gulf of Alaska and the North Pacific, will provide incremental improvements to the forecasting capability of AMIC in the future.

Acknowledgments. This research was carried out with support of the National Oceanic and Atmospheric Administration (NOAA) Great Lakes Environmental Research Laboratory (GLERL), awarded to the Cooperative Institute for Great Lakes Research (CIGLR) through the NOAA Cooperative Agreement with the University of Michigan (NA17OAR4320152). This is GLERL contribution 2004 and CIGLR contribution 1194.

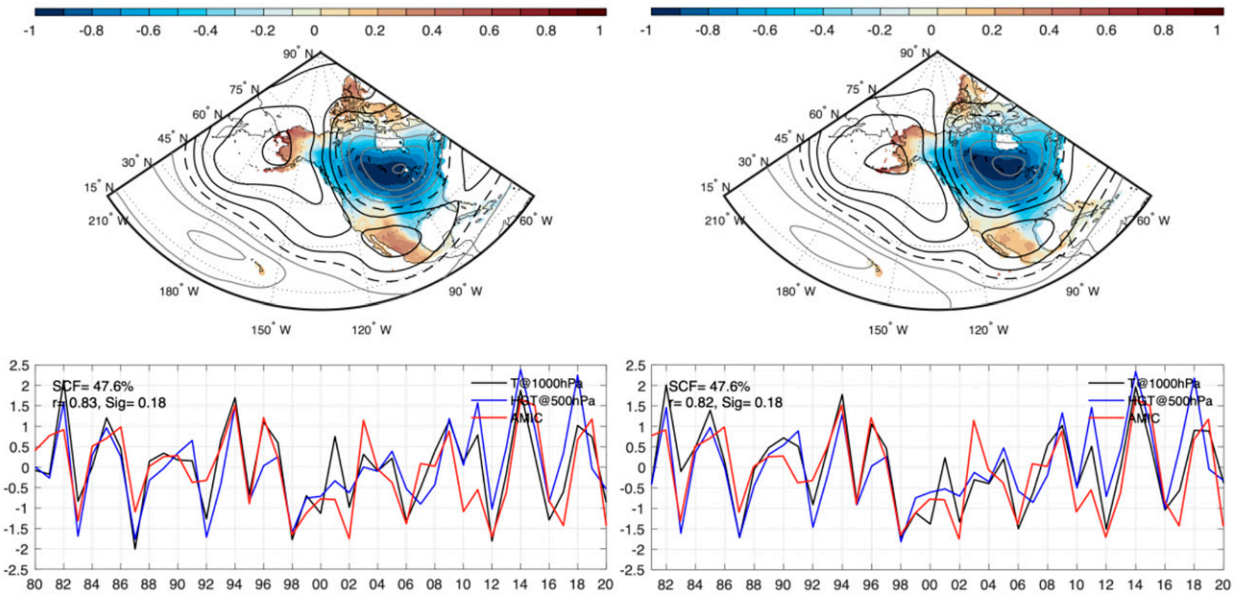

FIG. A1. Mode 1 results of SVD analyses on geopotential height at 500 hPa (Φ500) and surface air temperature at 2-m height (T_{2m}) from (left) ERA5 and (right) MERRA-2 averaged for December–January from 1980 to 2020. The same SVD analyses for NCEP are shown in Fig. 3a. Contours are the spatial pattern of Φ500, and colors are the spatial pattern of T_{2m}. Expansion coefficients of T_{2m} ($EC1_{T2m}$) and Φ500 ($EC1_{\Phi 500}$) are shown in black and blue in the lower panels. The red line is the AMIC time series.

Data availability statement. The annual maximum ice cover (AMIC) of the Great Lakes is obtained from the NOAA Great Lakes Environmental Research Laboratory (https://www.glerl.noaa.gov/data/ice/#historical). The monthly gridded Arctic sea ice concentration can be accessed at the National Snow and Ice Data Center (https://nsidc.org/data/g10010). The atmospheric data can be accessed at NCEP Gridded Climate Datasets (https://psl.noaa.gov/data/gridded/data.ncep.reanalysis2.html). The climate indices can be accessed at NOAA Climate Prediction Center (https://www.cpc.ncep.noaa.gov/data/teledoc/telecontents.shtml) and ESRL/PSL GEFS Reforecast 2 (https://psl.noaa.gov/data/climateindices/list/).

APPENDIX

Results from ERA5 and MERRA-2

Figure A1 displays the SVD analyses of geopotential height at 500 hPa and surface air temperature at 2-m height obtained from ERA5 and MERRA-2.

REFERENCES

Assel, R. A., 1992: Great Lakes winter-weather 700-hPa PNA teleconnections. *Mon. Wea. Rev.*, **120**, 2156–2163, https://doi.org/10.1175/1520-0493(1992)120<2156:GLWWHP>2.0.CO;2.

——, 1998: The 1997 ENSO event and implication for North American Laurentian Great Lakes winter severity and ice cover. *Geophys. Res. Lett.*, **25**, 1031–1033, https://doi.org/10.1029/98GL00720.

——, and D. M. Robertson, 1995: Changes in winter air temperatures near Lake Michigan, 1851–1993, as determined from regional lake-ice records. *Limnol. Oceanogr.*, **40**, 165–176, https://doi.org/10.4319/lo.1995.40.1.0165.

——, and S. Rodionov, 1998: Atmospheric teleconnections for annual maximum ice cover on the Laurentian Great Lakes. *Int. J. Climatol.*, **18**, 425–442, https://doi.org/10.1002/(SICI)1097-0088(19980330)18:4<425::AID-JOC258>3.0.CO;2-Q.

——, C. R. Snider, and R. Lawrence, 1985: Comparison of 1983 Great Lakes winter weather and ice conditions with previous years. *Mon. Wea. Rev.*, **113**, 291–303, https://doi.org/10.1175/1520-0493(1985)113<0291:COGLWW>2.0.CO;2.

——, J. E. Janowiak, S. Young, and D. Boyce, 1996: Winter 1994 weather and ice conditions for the Laurentian Great Lakes. *Bull. Amer. Meteor. Soc.*, **77**, 71–88, https://doi.org/10.1175/1520-0477(1996)077<0071:WWAICF>2.0.CO;2.

——, ——, D. Boyce, F. H. Quinn, and D. C. Norton, 2000: Laurentian Great Lakes ice and weather conditions for the 1998 El Niño winter. *Bull. Amer. Meteor. Soc.*, **8**, 703–718, https://doi.org/10.1175/1520-0477(2000)081<0703:LGLIAW>2.3.CO;2.

——, K. Cronk, and D. Norton, 2003: Recent trends in Laurentian Great Lakes ice cover. *Climatic Change*, **57**, 185–204, https://doi.org/10.1023/A:1022140604052.

——, S. Drobrot, and T. E. Croley, 2004: Improving 30-day Great Lakes ice cover outlooks. *J. Hydrometeor.*, **5**, 713–717, https://doi.org/10.1175/1525-7541(2004)005<0713:IDGLIC>2.0.CO;2.

Bai, X., and J. Wang, 2012: Atmospheric teleconnection patterns associated with severe and mild ice cover on the Great Lakes, 1963–2011. *Water Qual. Res. J.*, **47**, 421–435, https://doi.org/10.2166/wqrjc.2012.009.

——, ——, C. Sellinger, A. Clites, and R. Assel, 2012: Interannual variability of Great Lakes ice cover and its relationship to NAO and ENSO. *J. Geophys. Res.*, **117**, C03002, https://doi.org/10.1029/2010JC006932.

Barnes, E. A., 2013: Revisiting the evidence linking Arctic amplification to extreme weather in midlatitudes. *Geophys. Res. Lett.*, **40**, 4734–4739, https://doi.org/10.1002/grl.50880.

——, and L. M. Polvani, 2015: CMIP5 projections of Arctic amplification, of the North American/North Atlantic circulation, and of their relationship. *J. Climate*, **28**, 5254–5271, https://doi.org/10.1175/JCLI-D-14-00589.1.

Barnston, A. G., and R. E. Livezey, 1987: Classification, seasonality and persistence of low-frequency atmospheric circulation patterns. *Mon. Wea. Rev.*, **115**, 1083–1126, https://doi.org/10.1175/1520-0493(1987)115<1083:CSAPOL>2.0.CO;2.

——, M. Chelliah, and S. B. Goldenberg, 1997: Documentation of a highly ENSO-related SST region in the equatorial Pacific: Research note. *Atmos.–Ocean*, **35**, 367–383, https://doi.org/10.1080/07055900.1997.9649597.

Blackport, R., and J. A. Screen, 2020: Insignificant effect of Arctic amplification on the amplitude of midlatitude atmospheric waves. *Sci. Adv.*, **6**, eaay2880, https://doi.org/10.1126/sciadv.aay2880.

——, ——, K. van der Wiel, and R. Bintanja, 2019: Minimal influence of reduced Arctic sea ice on coincident cold winters in mid-latitudes. *Nat. Climate Change*, **9**, 697–704, https://doi.org/10.1038/s41558-019-0551-4.

Bond, N. A., M. F. Cronin, H. Freeland, and N. Mantua, 2015: Causes and impacts of the 2014 warm anomaly in the NE Pacific. *Geophys. Res. Lett.*, **42**, 3414–3420, https://doi.org/10.1002/2015GL063306.

Budikova, D., T. W. Ford, and J. D. Wright, 2021: Characterizing winter season severity in the Midwest United States, part II: Interannual variability. *Int. J. Climatol.*, **42**, 3499–3516, https://doi.org/10.1002/joc.7429.

Cai, Q., J. Wang, D. Beletsky, J. E. Overland, M. Ikeda, and L. Wan, 2021: Accelerated decline of summer Arctic sea ice during 1850–2017 and the amplified Arctic warming during the recent decades. *Environ. Res. Lett.*, **16**, 034015, https://doi.org/10.1088/1748-9326/abdb5f.

Cattiaux, J., Y. Peings, D. Saint-Martin, N. Trou-Kechout, and S. J. Vavrus, 2016: Sinuosity of midlatitude atmospheric flow in a warming world. *Geophys. Res. Lett.*, **43**, 8259–8268, https://doi.org/10.1002/2016GL070309.

Chen, G., J. Lu, D. A. Burrows, and L. R. Leung, 2015: Local finite-amplitude wave activity as an objective diagnostic of midlatitude extreme weather. *Geophys. Res. Lett.*, **42**, 10 952–10 960, https://doi.org/10.1002/2015GL066959.

Chhak, K. C., E. Di Lorenzo, N. Schneider, and P. F. Cummins, 2009: Forcing of low-frequency ocean variability in the northeast Pacific. *J. Climate*, **22**, 1255–1276, https://doi.org/10.1175/2008JCLI2639.1.

Cohen, J., and Coauthors, 2014: Recent Arctic amplification and extreme mid-latitude weather. *Nat. Geosci.*, **7**, 627–637, https://doi.org/10.1038/ngeo2234.

Deser, C., and M. L. Blackmon, 1995: On the relationship between tropical and North Pacific sea-surface temperature variations. *J. Climate*, **8**, 1677–1680, https://doi.org/10.1175/1520-0442(1995)008<1677:OTRBTA>2.0.CO;2.

Di Lorenzo, E., and Coauthors, 2008: North Pacific Gyre Oscillation links ocean climate and ecosystem change. *Geophys. Res. Lett.*, **35**, L08607, https://doi.org/10.1029/2007GL032838.

——, G. Liguori, N. Schneider, J. C. Furtado, B. T. Anderson, and M. A. Alexander, 2015: ENSO and meridional modes: A null hypothesis for Pacific climate variability. *Geophys. Res. Lett.*, **42**, 9440–9448, https://doi.org/10.1002/2015GL066281.

Ding, H., R. J. Greatbatch, M. Latif, W. Park, and R. Gerdes, 2013: Hindcast of the 1976/77 and 1998/99 climate shifts in the Pacific. *J. Climate*, **26**, 7650–7661, https://doi.org/10.1175/JCLI-D-12-00626.1.

Francis, J. A., and S. J. Vavrus, 2012: Evidence linking Arctic amplification to extreme weather in mid-latitudes. *Geophys. Res. Lett.*, **39**, L06801, https://doi.org/10.1029/2012GL051000.

——, W. Chan, D. J. Leathers, J. R. Miller, and D. E. Veron, 2009: Winter Northern Hemisphere weather patterns remember summer Arctic sea-ice extent. *Geophys. Res. Lett.*, **36**, L07503, https://doi.org/10.1029/2009GL037274.

Furtado, J. C., E. Di Lorenzo, B. T. Anderson, and N. Schneider, 2012: Linkages between the North Pacific Oscillation and central tropical Pacific SSTs at low frequencies. *Climate Dyn.*, **39**, 2833–2846, https://doi.org/10.1007/s00382-011-1245-4.

Gelaro, R., and Coauthors, 2017: The Modern-Era Retrospective Analysis for Research and Applications, version 2 (MERRA-2). *J. Climate*, **30**, 5419–5454, https://doi.org/10.1175/JCLI-D-16-0758.1.

Gershunov, A., and T. P. Barnett, 1998: Interdecadal modulation of ENSO teleconnections. *Bull. Amer. Meteor. Soc.*, **79**, 2715–2726, https://doi.org/10.1175/1520-0477(1998)079<2715:IMOET>2.0.CO;2.

Guan, W., X. Jiang, X. Ren, G. Chen, and Q. Ding, 2021: Pacific sea surface temperature anomalies as important boundary forcing in driving the interannual warm Arctic–cold continent pattern over the North American sector. *J. Climate*, **34**, 5923–5937, https://doi.org/10.1175/JCLI-D-20-0867.1.

Hanson, H. P., C. S. Hanson, and B. H. Yoo, 1992: Recent Great Lakes ice trends. *Bull. Amer. Meteor. Soc.*, **73**, 577–584, https://www.jstor.org/stable/26229815.

Hartmann, D. L., 2015: Pacific sea surface temperature and the winter of 2014. *Geophys. Res. Lett.*, **42**, 1894–1902, https://doi.org/10.1002/2015GL063083.

Hersbach, H., and Coauthors, 2020: The ERA5 global reanalysis. *Quart. J. Roy. Meteor. Soc.*, **146**, 1999–2049, https://doi.org/10.1002/qj.3803.

Honda, M., J. Inoue, and S. Yamane, 2009: Influence of low Arctic sea-ice minima on anomalously cold Eurasian winters. *Geophys. Res. Lett.*, **36**, L08707, https://doi.org/10.1029/2008GL037079.

Huntingford, C., and Coauthors, 2015: Reply to 'Drivers of the 2013/14 winter floods in the UK'. *Nat. Climate Change*, **5**, 491–492, https://doi.org/10.1038/nclimate2613.

Hurrell, J. W., 1995: Decadal trends in the North Atlantic Oscillation: Regional temperatures and precipitation. *Science*, **269**, 676–679, https://doi.org/10.1126/science.269.5224.676.

Johnstone, J. A., and N. J. Mantua, 2014: Atmospheric controls on northeast Pacific temperature variability and change, 1900–2012. *Proc. Natl. Acad. Sci. USA*, **111**, 14 360–14 365, https://doi.org/10.1073/pnas.1318371111.

Kanamitsu, M., W. Ebisuzaki, J. Woollen, S.-K. Yang, J. J. Hnilo, M. Fiorino, and G. L. Potter, 2002: NCEP–DOE AMIP-II Reanalysis (R-2). *Bull. Amer. Meteor. Soc.*, **83**, 1631–1644, https://doi.org/10.1175/BAMS-83-11-1631.

Kodera, K., H. Mukougawa, P. Maury, M. Ueda, and C. Claud, 2015: Absorbing and reflecting sudden stratospheric warming events and their relationship with tropospheric circulation. *J. Geophys. Res. Atmos.*, **121**, 80–94, https://doi.org/10.1002/2015JD023359.

Kretschmer, M., J. Cohen, V. Matthias, J. Runge, and D. Coumou, 2018: The different stratospheric influence on cold-extremes

in Eurasia and North America. *npj Climate Atmos. Sci.*, **1**, 44, https://doi.org/10.1038/s41612-018-0054-4.

Kug, J.-S., J.-H. Jeong, Y.-S. Jang, B.-M. Kim, C. K. Folland, S.-K. Min, and S.-W. Son, 2015: Two distinct influences of Arctic warming on cold winters over North America and East Asia. *Nat. Geosci.*, **8**, 759–762, https://doi.org/10.1038/ngeo2517.

Lee, M., C. Hong, and H. Hsu, 2015: Compounding effects of warm sea surface temperature and reduced sea ice on the extreme circulation over the extratropical North Pacific and North America during the 2013–2014 boreal winter. *Geophys. Res. Lett.*, **42**, 1612–1618, https://doi.org/10.1002/2014GL062956.

Liang, Y.-C., J.-Y. Yu, E. S. Saltzman, and F. Wang, 2017: Linking the tropical Northern Hemisphere pattern to the Pacific warm blob and Atlantic cold blob. *J. Climate*, **30**, 9041–9057, https://doi.org/10.1175/JCLI-D-17-0149.1.

Linkin, M. E., and S. Nigam, 2008: The North Pacific oscillation–west Pacific teleconnection pattern: Mature-phase structure and winter impacts. *J. Climate*, **21**, 1979–1997, https://doi.org/10.1175/2007JCLI2048.1.

Liu, J., J. A. Curry, H. Wang, M. Song, and R. M. Horton, 2012: Impact of declining Arctic sea ice on winter snowfall. *Proc. Natl. Acad. Sci. USA*, **109**, 4074–4079, https://doi.org/10.1073/pnas.1114910109.

Magnuson, J. J., 2000: Historical trends in lake and river ice cover in the Northern Hemisphere. *Science*, **289**, 1743–1746, https://doi.org/10.1126/science.289.5485.1743.

——, and Coauthors, 1995: Region 1—Laurentian Great Lakes and Precambrian Shield. *Regional Assessment of Freshwater Ecosystems and Climate Change in North America*, U.S. Environmental Protection Agency and U.S. Geological Survey, 3–4.

Mantua, N. J., S. R. Hare, Y. Zhang, J. M. Wallace, and R. C. Francis, 1997: A Pacific interdecadal climate oscillation with impacts on salmon production. *Bull. Amer. Meteor. Soc.*, **78**, 1069–1080, https://doi.org/10.1175/1520-0477(1997)078<1069:APICOW>2.0.CO;2.

Marinaro, A., S. Hilberg, D. Changnon, and J. R. Angel, 2015: The North Pacific–driven severe Midwest winter of 2013/14. *J. Appl. Meteor. Climatol.*, **54**, 2141–2151, https://doi.org/10.1175/JAMC-D-15-0084.1.

Mo, K. C., and R. E. Livezey, 1986: Tropical–extratropical geopotential height teleconnections during the Northern Hemisphere winter. *Mon. Wea. Rev.*, **114**, 2488–2515, https://doi.org/10.1175/1520-0493(1986)114<2488:TEGHTD>2.0.CO;2.

Niimi, A. J., 1982: Economic and environmental issues of the proposed extension of the winter navigation season and improvements on the Great Lakes–St. Lawrence Seaway system. *J. Great Lakes Res.*, **8**, 532–549, https://doi.org/10.1016/S0380-1330(82)71991-4.

Ogi, M., B. Taguchi, M. Honda, D. G. Barber, and S. Rysgaard, 2015: Summer-to-winter sea-ice linkage between the Arctic Ocean and the Okhotsk Sea through atmospheric circulation. *J. Climate*, **28**, 4971–4979, https://doi.org/10.1175/JCLI-D-14-00297.1.

Overland, J. E., K. R. Wood, and M. Wang, 2011: Warm Arctic–cold continents: Climate impacts of the newly open Arctic sea. *Polar Res.*, **30**, 15787, https://doi.org/10.3402/polar.v30i0.15787.

——, and Coauthors, 2021: How do intermittency and simultaneous processes obfuscate the Arctic influence on midlatitude winter extreme weather events? *Environ. Res. Lett.*, **16**, 043002, https://doi.org/10.1088/1748-9326/abdb5d.

Ozersky, T., and Coauthors, 2021: The changing face of winter: Lessons and questions from the Laurentian Great Lakes. *J. Geophys. Res. Biogeosci.*, **126**, e2021JG006247, https://doi.org/10.1029/2021JG006247.

Park, J.-Y., S.-W. Yeh, and J.-S. Kug, 2012: Revisited relationship between tropical and North Pacific sea surface temperature variations. *Geophys. Res. Lett.*, **39**, L02703, https://doi.org/10.1029/2011GL050005.

Power, S., F. Tseitkin, S. J. Torok, B. Lavery, R. Dahni, and B. McAvaney, 1998: Australian temperature, Australian rainfall and the Southern Oscillation, 1910–1992: Coherent variability and recent changes. *Aust. Meteor. Mag.*, **47**, 85–101.

Rayner, N. A., D. E. Parker, E. B. Horton, C. K. Folland, L. V. Alexander, D. P. Rowell, E. C. Kent, and A. Kaplan, 2003: Global analyses of sea surface temperature, sea ice, and night marine air temperature since the late nineteenth century. *J. Geophys. Res.*, **108**, 4407, https://doi.org/10.1029/2002JD002670.

Rodionov, S., and R. Assel, 2000: Atmospheric teleconnection patterns and severity of winters in the Laurentian Great Lakes basin. *Atmos.–Ocean*, **38**, 601–635, https://doi.org/10.1080/07055900.2000.9649661.

——, and ——, 2001: A new look at the Pacific/North American Index. *Geophys. Res. Lett.*, **28**, 1519–1522, https://doi.org/10.1029/2000GL012185.

Rogers, J. C., 1976: Long-range forecasting of maximum ice extent on the Great Lakes. NOAA Tech. Memo. ERL-GLERL-007, 18 pp., https://repository.library.noaa.gov/view/noaa/11020.

Röthlisberger, M., S. Pfahl, and O. Martius, 2016: Regional-scale jet waviness modulates the occurrence of midlatitude weather extremes. *Geophys. Res. Lett.*, **43**, 10 989–10 997, https://doi.org/10.1002/2016GL070944.

Smith, E. T., and S. C. Sheridan, 2021: The relationship between teleconnections, surface temperature, and cold air outbreaks. *Int. J. Climatol.*, **42**, 1531–1543, https://doi.org/10.1002/joc.7318.

Smith, J. B., 1991: The potential impacts of climate change on the Great Lakes. *Bull. Amer. Meteor. Soc.*, **72**, 21–28, https://doi.org/10.1175/1520-0477(1991)072<0021:TPIOCC>2.0.CO;2.

Takaya, K., and H. Nakamura, 2001: A formulation of a phase-independent wave-activity flux for stationary and migratory quasigeostrophic eddies on a zonally varying basic flow. *J. Atmos. Sci.*, **58**, 608–627, https://doi.org/10.1175/1520-0469(2001)058<0608:AFOAPI>2.0.CO;2.

Thompson, D. W. J., and J. M. Wallace, 1998: The Arctic oscillation signature in the wintertime geopotential height and temperature fields. *Geophys. Res. Lett.*, **25**, 1297–1300, https://doi.org/10.1029/98GL00950.

Titze, D. J., and J. A. Austin, 2014: Winter thermal structure of Lake Superior. *Limnol. Oceanogr.*, **59**, 1336–1348, https://doi.org/10.4319/lo.2014.59.4.1336.

Van Cleave, K., J. D. Lenters, J. Wang, and E. M. Verhamme, 2014: A regime shift in Lake Superior ice cover, evaporation, and water temperature following the warm El Niño winter of 1997–1998. *Limnol. Oceanogr.*, **59**, 1889–1898, https://doi.org/10.4319/lo.2014.59.6.1889.

Vanderploeg, H. A., S. J. Bolsenga, G. L. Fahnenstiel, J. R. Liebig, and W. S. Gardner, 1992: Plankton ecology in an ice-covered bay of Lake Michigan: Utilization of a winter phytoplankton bloom by reproducing copepods. *Hydrobiologia*, **243**, 175–183, https://doi.org/10.1007/BF00007033.

Vavrus, S. J., F. Wang, J. E. Martin, J. A. Francis, Y. Peings, and J. Cattiaux, 2017: Changes in North American atmospheric circulation and extreme weather: Influence of Arctic

amplification and Northern Hemisphere snow cover. *J. Climate*, **30**, 4317–4333, https://doi.org/10.1175/JCLI-D-16-0762.1.

Wang, J., X. Bai, G. Leshkevich, M. Colton, A. Clites, and B. Lofgren, 2010: Severe ice cover on Great Lakes during winter 2008–2009. *Eos, Trans. Amer. Geophys. Union*, **91**, 41–42, https://doi.org/10.1029/2010EO050001.

——, ——, H. Hu, A. Clites, M. Colton, and B. Lofgren, 2012: Temporal and spatial variability of Great Lakes ice cover, 1973–2010. *J. Climate*, **25**, 1318–1329, https://doi.org/10.1175/2011JCLI4066.1.

——, J. Kessler, F. Hang, H. Hu, A. H. Clites, and P. Chu, 2017: Great Lakes ice climatology update of winters 2012–2017: Seasonal cycle, interannual variability, decadal variability, and trend for the period 1973–2017. NOAA Tech. Memo. GLERL-170, 14 pp., https://www.glerl.noaa.gov/pubs/tech_reports/glerl-170/tm-170.pdf.

——, and Coauthors, 2018: Decadal variability of Great Lakes ice cover in response to AMO and PDO, 1963–2017. *J. Climate*, **31**, 7249–7268, https://doi.org/10.1175/JCLI-D-17-0283.1.

——, T.-Y. Yang, J. Kessler, H. Hu, and P. Chu, 2020: Great Lakes ice duration, winter severity index, cumulative freezing degree days, and atmospheric teleconnection patterns, 1973–2018. NOAA Tech. Memo. GLERL-174, 67 pp., https://doi.org/10.25923/88c9-hm22.

Wang, S.-Y., L. Hipps, R. R. Gillies, and J.-H. Yoon, 2014: Probable causes of the abnormal ridge accompanying the 2013–2014 California drought: ENSO precursor and anthropogenic warming footprint. *Geophys. Res. Lett.*, **41**, 3220–3226, https://doi.org/10.1002/2014GL059748.

——, W.-R. Huang, and J.-H. Yoon, 2015: The North American winter 'dipole' and extremes activity: A CMIP5 assessment. *Atmos. Sci. Lett.*, **16**, 338–345, https://doi.org/10.1002/asl2.565.

Wilcoxon, F., 1945: Individual comparisons by ranking methods. *Biom. Bull.*, **1**, 80–83, https://doi.org/10.2307/3001968.

Yang, T.-Y., J. Kessler, L. Mason, P. Y. Chu, and J. Wang, 2020: A consistent Great Lakes ice cover digital data set for winters 1973–2019. *Sci. Data*, **7**, 259, https://doi.org/10.1038/s41597-020-00603-1.

Zhang, P., Y. Wu, I. R. Simpson, K. L. Smith, X. Zhang, B. De, and P. Callaghan, 2018: A stratospheric pathway linking a colder Siberia to Barents-Kara Sea sea ice loss. *Sci. Adv.*, **4**, eaat6025, https://doi.org/10.1126/sciadv.aat6025.

Zhang, Y., J. M. Wallace, and D. S. Battisti, 1997: ENSO-like interdecadal variability: 1900–93. *J. Climate*, **10**, 1004–1020, https://doi.org/10.1175/1520-0442(1997)010<1004:ELIV>2.0.CO;2.